Growth and advanced characterization of solution-derived nanoscale $La_{0.7}Sr_{0.3}MnO_3$ heteroepitaxial systems

Jone Zabaleta Llorens

Departament de Materials Superconductors i Nanoestructuració a Gran Escala, ICMAB-CSIC
Supervisors: Prof. T. Puig Molina and Dr. N. Mestres Andreu
Tutor: Prof. A. Sánchez Moreno

Departament de Física
Programa de Ciència de Materials
Universitat Autònoma de Barcelona

Bellaterra, December 2011

Chapter 4

Magnetic structure of LSMO nanoislands

As concluded from Chapter 3, $La_{0.7}Sr_{0.3}MnO_3$ (LSMO) nanoislands on YSZ single crystals exhibit magnetization values and Curie temperature close to the bulk LSMO values reported in the literature. However, the magnetic properties of individual islands are not accessible via macroscopic techniques like SQUID magnetometry. Not at least in the case of a system encompassing a broad variety of island size and morphologies, like the solution-derived LSMO nanostructures we have discussed. In the present chapter we explore the individual magnetic structure of the LSMO nanoislands grown on YSZ. For this purpose we exploit the capabilities of Magnetic Force Microscopy (MFM), performed in air and at room temperature.

Since in the late 80s Martin and Wickramasinghe [219] and separately Sáenz and coworkers [220] first adapted an Atomic Force Microscope to image magnetic fields and magnetic domains, MFM has become a routinely used technique for characterizing magnetic samples at the submicrometre scale. Domain walls, ferromagnetic domain patterns, and magnetic vortices are some of the phenomena that can be studied by means of MFM. Besides, this is a flexible technique that supports operation under tunable conditions like high vacuum and low temperature. Meanwhile, it can be easily operated in air and at room temperature, as we have done, taking advantage of the high T_C value of our system of ferromagnetic (FM) nanoislands. An additional fact, essential for us, is that insulating samples can be imaged without difficulties. This is in clear contrast with other techniques such as Photoemission Electron Microscopy (PEEM), where the insulating substrate is a limiting factor, as we will discuss in Chapter 5. The main drawback of MFM is the lateral resolution, which in our conditions turned out to be around 50 nm. Also, it remains mainly a qualitative tool: the magnetic contrast we measure is proportional to the gradient of the force between tip and sample. Hence, to obtain a mapping of the field distribution, one would need to perform a double integration with well-defined boundary conditions, and know the exact characteristics of the tip. This is why imaging magnetic samples is not as difficult as interpreting the results, and also the reason why significant efforts are now directed towards correlating the MFM observations to possible magnetic landscapes via numerical simulations.

After a brief Introduction to the MFM technique, the present chapter describes the

tuning of the experimental parameters to our system of self-assembled LSMO nanoislands. The crucial role of the tip for successful MFM imaging is emphasized. Doing so permits unveiling aspects of the system that could otherwise be easily disregarded. In particular, we will see that different nanoisland size and morphologies exhibit different magnetic structures. We will be able to draw a complete magnetic phase diagram in which the vortex state occupies a central role. As this is the first time vortex states have been imaged by MFM in sub 200 nm wide LSMO islands, we have carried out a thorough analysis of our observations, trying to contextualize them in the framework of existing experimental results and analytical and micromagnetic models. Finally, we will conclude with a brief summary and point out the open questions that will likely motivate future work on this topic.

4.1 Basics on MFM

In Magnetic Force Microscopy (MFM), a sharp magnetized tip is scanned over the sample surface, while held a few tens of nm away from it. As a type of Scanning Probe Microscopy (SPM), in MFM the tip is the probe which senses the interaction due to tip-sample forces, in this case magnetic forces. A fundamental point here is to be able to discern magnetic interactions from the whole range of simultaneous forces interacting between the tip and the sample (attractive Van der Waals, repulsive Pauli interaction, electrostatic forces, capillary and adhesion forces...). Some forces are short range while others, like magnetic forces, are long range [see Fig.4.1 (a)]. Tuning the tip to sample distance may thus help disentangle the interactions at play. The *nm* range distance between the tip and the sample enables sensing very small forces in the $10^{-13}-10^{-5}$ N range [221]. To know the particular characteristics of the material under investigation will also be relevant to interpret the data. These issues are generally addressed using different measuring modes and tuning the particular electronics of the feedback system.

In the *Dynamic Operation* mode used in our measurements, the sharp tip is set to oscillate at the resonance frequency of the small cantilever, to the end of which the tip is attached. This free oscillation frequency is determined by the force constant of the cantilever k (determined, in turn, by its geometrical and mechanical parameters). When the tip approaches the sample surface, however, the perturbation sensed by the oscillating tip will affect its motion: a shift in the amplitude A, frequency ω, and phase ϕ occurs [222]. Such displacements in A, ω and ϕ reflect the magnitude and the attractive/repulsive nature of the interaction between tip and sample. The variations of the tip oscillation are detected by the deviation of a laser beam focused on the tip (optical detection mode) and quantified using the appropriate lock-in techniques. In the case of small external forces, the $|\vec{F}^{ext}|$ is treated as a perturbation that causes the cantilever to have an effective force constant $k_{eff} = k - \partial F_z^{ext}/\partial z$, where we take only the direction of the tip-sample distance z, i.e. $|\vec{F}^{ext}| = F_z^{ext}$. Eqs. 4.1, 4.2 and 4.3 below show the expressions of the shift in A, ω and ϕ caused by such external force.

$$\Delta A \propto \frac{Q}{2k}\frac{\partial F_z^{ext}}{\partial z} \tag{4.1}$$

$$\Delta\omega = \omega - \omega_0 = -\frac{\omega_0}{2k}\frac{\partial F_z^{ext}}{\partial z} \tag{4.2}$$

$$\tan\phi = \frac{\omega\omega_0}{Q(\omega^2-\omega_0^2)} \tag{4.3}$$

where Q is the Quality factor of the oscillation, k is the force constant of the cantilever, ω_0 its resonance frequency and z the oscillation direction.

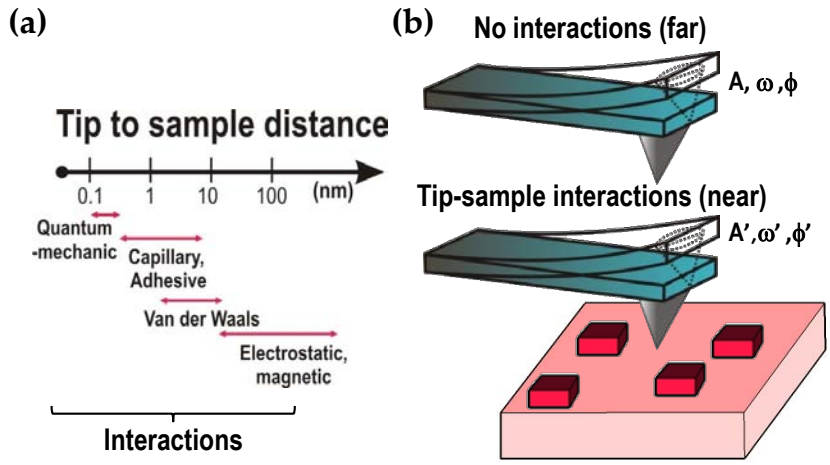

Fig. 4.1: *(a) Scheme of the distance range at which different tip-sample interactions are present. (b) Sketch of the oscillating cantilever with the tip at its end; far from the substrate (above) and near the substrate (below) where the tip-sample forces change the amplitude, frequency and phase of the oscillation.*

Using A, ω or ϕ as feedback parameters we can register the shifts with respect to a certain electronic set-point and react to make such shift equal to zero. Such 'reaction' is achieved by the expansion or contraction of the piezoelectric tubes that control the tip-sample distance. This way, if the amplitude A is the selected feedback parameter for measuring the topography signal, our topography image will be a constant amplitude image where the expansion/contraction of the piezo is registered. The stronger the interaction, the stronger the shift in A will be and the more the piezo will expand or contract. This is evidenced in an enhanced contrast in the topography image.

As commented before, it is not trivial to interpret the forces that produce the measured shifts because all kind of interactions are generally present. For the particular case of magnetic forces, the energy at a distance $\vec{r}$ between the magnetic tip and the sample may be written as [223]:

$$E(\vec{r}) = -\mu_0 \int_{tip} [\vec{M}_{tip}(\vec{r'})\ \vec{H}_{sample}(\vec{r}+\vec{r'})]\mathrm{d}^3\vec{r'} \tag{4.4}$$

where $\vec{M}_{tip}(\vec{r'})$ is the tip magnetization at the $\vec{r'}$ coordinate within the magnetic coating of the tip, $\mathrm{d}^3\vec{r'}$ is the coating unit volume, and $\vec{H}_{sample}(\vec{r}+\vec{r'})$ is the stray field produced by the magnetic sample at that point of the tip. In other words, the magnetic interaction between the tip and the sample is determined by the convolution of the tip magnetization and the stray field of the sample. Note that we would obtain an equivalent expression by swapping the subscripts in 4.4 and extend the integral for the sample volume elements. Such energy produces a force between the tip and the sample (Eq. 4.5) which gradient is proportional to the measured shift in our amplitude, frequency or phase parameters, following what we saw in Eqs. 4.1, 4.2 and 4.3.

$$\vec{F}^{ext}(\vec{r}) = -\vec{\nabla}E(\vec{r}) \tag{4.5}$$

The exact expression for the force will depend on the specific forms of $\vec{M}_{tip}$ and $\vec{H}_{sample}$

for different magnetic materials, geometries...etc and it is far from being trivial. A good number of models have been proposed in particular cases for the force between the magnetic sample and tip [224, 225, 225–229]. For the case of a tip modeled as a dipole with magnetic moment $\vec{m}$, the expression 4.5 takes the form [226]:

$$\vec{F}^{ext}(\vec{r}) = \mu_0 \vec{\nabla}(\vec{m} \cdot \vec{H}) \tag{4.6}$$

and the force gradient, proportional to the A, ω and ϕ shifts, will thus be

$$\frac{\partial F_z^{ext}}{\partial z} = \mu_0 \vec{m} \frac{\partial^2 \vec{H}}{\partial z^2} \tag{4.7}$$

in which we took the tip magnetic moment $\vec{m}$ to be independent of z. Accordingly, the MFM contrast we measure, given by the shifts of the oscillating parameters of our cantilever (Eqs. 4.1, 4.2 and 4.3), is proportional to the stray field variation in the direction perpendicular to the sample surface. Note again that only the z component of the force has been written. We are here assuming that our MFM signal comes only from the variation of the force component along the perpendicular direction, which is generally a reasonable approximation since the cantilever oscillation is along z. The nanometric tip radius is responsible for nanoscale lateral and vertical resolution [230].

Along with the variation of the stray field of the sample, the magnetic dipole $|\vec{m}|$ representing the tip in Eq. 4.7, plays a role too in the origin of the measured magnetic contrast. Moreover, in real experiments, the choice of the magnetic tip is particularly important: we may or may not be able to measure the same sample depending on the magnetic characteristics of the selected tip. For instance, a tip with a strong magnetic moment may modify the domain structure of the measured sample, while one with a weak magnetic moment may be altered by the stray field of a strong magnetic sample. In either case, the contrast obtained from the measurement will not be representative of the specific sample, and data interpretation will hence require special care. The ideal situation for a *non-destructive MFM operation* was expressed by Hartmann in terms of the relative values of anisotropy fields H_K and the saturation magnetization values M_S of tip and sample [224]:

$$\frac{H_K^{samp}}{M_S^{tip}} \geq 1 \tag{4.8}$$

$$\frac{H_K^{tip}}{M_S^{samp}} \geq 1 \tag{4.9}$$

By meeting these conditions we expect the MFM data to reliably reflect the original sample magnetic structure. However, they also imply that on a soft magnetic sample we are constrained to the use of tips of rather low magnetic moment, which can make the obtained signal too weak to be measured. This is why the appropriate choice of the tip is essential.

The study here presented was carried out in collaboration with Dr. Agustina Asenjo and Dr. Miriam Jaafar from the *Group of magnetism and magnetization processes* at the Instituto de Ciencia de Materiales de Madrid (ICMM-CSIC). I also profited from their expertise while working under their supervision in the context of a short 1 month stay in the course of my PhD thesis.

4.2 Experimental procedure: tuning the MFM operation on self-assembled LSMO nanoislands

4.2.1 Experimental set-up and measuring conditions. Magnetic contrast

The measurements were done using a commercial ambient AFM/MFM system from Nanotec Electrónica S.L, working at room temperature. This microscope was appropriately modified by M. Jaafar as part of her PhD work to be able to apply constant in-plane and out-of-plane magnetic field while imaging the sample. A detailed description of the system is given in her thesis [231] and in the corresponding article [232]. Our main goal is to learn what the micromagnetic structure of individual islands is, and how their magnetic domain configuration varies under applied field. A great number of experiments were done in remanence, a few with out-of-plane applied magnetic field, and some with in-plane magnetic field. Details on the out-of-plane set-up can be found in the thesis by M. Jaafar [231]. The in-plane set-up, which we used more often, is sketched in Fig. 4.2. It consists of a copper electromagnet (0.5 mm diameter wire) connected to two iron bars that enclose the magnetic flux created by the coil and that are separated by an air gap. The sample is located between the ends of the iron pieces and the field intensity can be changed by changing their separation, with values from 4 to 8 mm. In our case, maximum fields of ∼45 mT were reached when applying a 2 A current flow through the coil. The *current* to *field* calibration is done systematically before a series of measurements, especially if the electromagnet is manipulated or the gap width changes. For such purpose we used a Hall probe (STB5X, 0.020”). A cooling system keeps the coil refrigerated. This is important because the current may flow for hours (every MFM image can take from 5 to 20 min to be completed). However, the large distance between the coil and the sample (∼13 cm) as well as the cooling system were proved to give very small temperature changes: a 3 K temperature rise was measured by the application of a 0.11 T field during 3 hr [231].

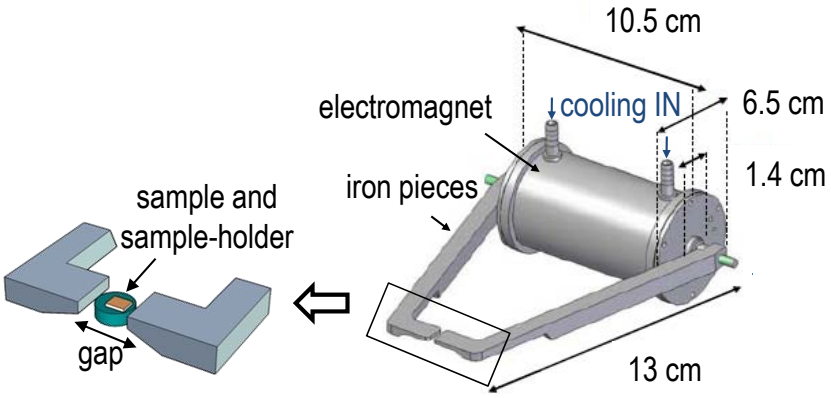

Fig. 4.2: *Schematic illustration of the coil system used for in-plane magnetic field application. Adapted from [231].*

MFM imaging was performed in the dynamic mode using the lift-mode operation, i.e. the oscillating cantilever was placed at two different distances from the sample surface for each scanned line: close to the surface (∼10 nm) first, for topography data acquisition, and far from the surface afterwards, for the magnetic signal collection, at typical retrace distances of 30-60 nm. In our particular case, after the topography measurement, the

piezoelectric tube, in charge of the tip-to-sample distance regulation, repeats the previous topography movements at the larger retrace distance. This way, the sample surface and the tip are maintained at a constant distance and we are able to exclude topography effects in the magnetic signal. Choosing the appropriate distance is essential in order to avoid topography crosstalk from the MFM image while keeping a good signal-to-noise ratio. We have used the oscillation amplitude A to track the topography signal. The magnetic interaction, in turn, is detected in the contrast measured in the phase shift channel, during the retrace scan. This so-called Amplitude modulation-AFM is the usual operating mode in air: small quality factors $Q \in$ [50-1000] yield the feedback in A while the functional properties of the materials are commonly mapped by recording the phase shift between the driving force and the tip oscillation [222].

In addition to the above, we have used a second feedback, known as the *Phase Locked Loop* (PLL), which is implemented in the Nanotec electronics and software. It works by changing the excitation frequency at which the cantilever is driven in order to keep the phase constant (at its resonance value $\frac{\pi}{2}$, usually). The phase shift being equal to zero, the information contained in the amplitude is solely due to its real part. In other words, we have no contribution from forces other than Van der Waals in the topography image (adhesion, capillary, and magnetic forces are left out). Since the phase shift is kept to zero, the magnetic interaction is recorded in terms of the frequency needed to make this phase shift zero. From Eq. 4.2 it follows that we will observe a positive shift in the frequency when repulsive forces are present, and, conversely, a negative shift when the attractive forces pull the cantilever closer to the surface.

Fig 4.3 shows the topography and the magnetic contrast images, (a) and (b) respectively, of an LSMO nanoisland ensemble grown on a (110)-oriented YSZ substrate. Since the feedback is done in amplitude (A), topography image is a constant A image, and the Amplitude image thus records the feedback error in trying to keep A constant. Similarly, we show the MFM image (recorded at a 30 nm retrace distance), shown as the excitation frequency given to the cantilever to keep the phase unchanged. The phase image is thus its corresponding error signal. The non-zero error signals are the typical obtained; we have enhanced the contrast in order to highlight them. At a first glance, the nanoisland ensemble appears as agglomerate bunches of poorly defined nanoislands. This is seen very clearly in the amplitude channel. In the MFM image, however, the magnetic contrast arises only from well-separated individual islands. By looking at the amplitude image more closely, we can correlate the original island to its corresponding magnetic contrast. The MFM image hence helps distinguishing magnetic islands and non-magnetic material attached to them.

Magnetic tips are saturated using a permanent magnet prior to imaging the sample. The tip is usually magnetized parallel to its axis, that is, perpendicular to the sample surface, which is done easily because of its large shape anisotropy. We may then take the magnetic moment of the tip to be $|\vec{m}| \sim m_z$. Bearing in mind that the magnetic contrast is proportional to the force gradient in z, we will then see the largest contrast in the regions with out-of-plane magnetization. Two representative examples of the MFM contrast obtained with out-of-plane and in-plane magnetized samples are given in Fig. 4.4 (taken from [231]). They correspond to (a), magnetic Ni nanowires (magnetization along their long axis $\pm z$) embedded in a porous alumina non-magnetic matrix, where the magnetic contrast comes from each of the wires; and (b), in-plane magnetic domains within a commercial hard disk drive track. The magnetic contrast there arises from the domain walls.

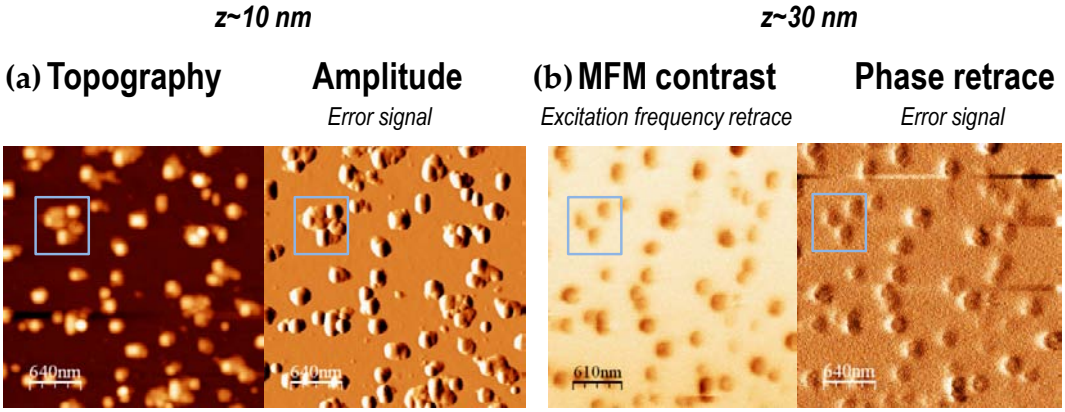

Fig. 4.3: *(a) Topography image (left) and the corresponding amplitude image (right) taken at z∼10 nm from the sample surface. The z bar comprehends 90 nm and 180 mV, respectively. (b) Excitation frequency image [magnetic contrast image (left)] and its corresponding phase image (right) taken at a retrace distance z∼30 nm from the sample surface. The z bar comprehends 4 Hz and 10 mV, respectively. The blue squares highlight that what seems agglomerated material in (a), are three distinct magnetic islands in reality, surrounded by non-magnetic dirt, as evidenced in (b).*

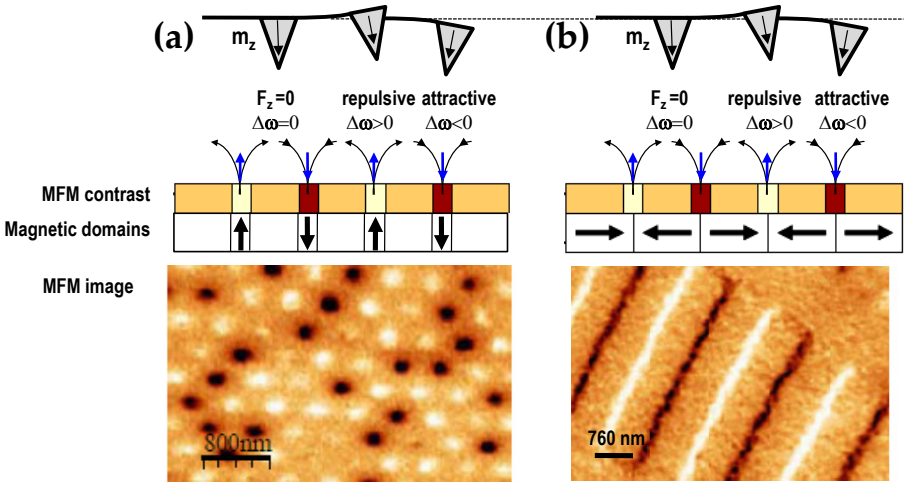

Fig. 4.4: *(a) Out-of-plane magnetized Ni nanowires embedded in a porous alumina matrix. (b) In-plane magnetized magnetic domains in a hard drive disk. The tip-sample attractive (repulsive) magnetic interaction reduces (enhances) the oscillation frequency, represented as a dark (bright) contrast against the non-magnetic background. Figure adapted from [231].*

4.2.2 Towards the optimal imaging of LSMO nanoislands: the role of the magnetic tip

The critical role of the magnetic tip in MFM imaging

Our CSD-derived LSMO nanoislands largely depart from the above paradigmatic examples of ferromagnetic in-plane and out-of-plane samples. From Chapter 3 we know that the magnetization of the nanoislands is comparable to the 590 emu/cm^3 of bulk LSMO at low temperature. We know as well that it falls down to 300$\pm$40 emu/cm^3 at 300 K. Besides, although we expect the nanoisland magnetization to lie in-plane, we cannot neglect the presence of non-zero out-of-plane component (recall the hysteresis cycles for LSMO on YSZ described in Chapter 3). In addition to a low magnetization, the small nanoisland volume implies a very small magnetic moment. While these averaged values do not account for the individual behavior of the nanoislands, they already point out that the tip-sample magnetic interaction will not be strong. As a soft ferromagnet with low coercive field, we may also expect the stray field of the magnetic tip to modify the nanoisland domain configuration. Keeping all this in mind, the first step in the MFM study was to check whether the magnetic signal could be measured at all, and whether this could be done without modifying the original magnetic structure of the nanoisland.

To this end, initially, experiments were performed by applying an out-of-plane magnetic field. Fig. 4.5 (a) displays the measured Amplitude image (i.e. the topography error) and Fig. 4.5 (b) the MFM image of the same area of a LSMO nanoisland ensemble grown on (001)-YSZ, which we shall call *Sample 1* hereafter. The MFM image was collected during the retrace scan under a magnetic field of 30 mT, applied perpendicular to the sample (parallel to the tip magnetization). We expect the 30 mT field to align many of the island magnetic moments parallel to the tip magnetic moment. This would then be reflected as a dark contrast at the island location. The amplitude image shows the faceted shape of the square-base nanoislands; also, the substrate is not completely clean, but covered with small islands. As we already remarked in Chapter 3, this may happen in some LSMO/YSZ nanostructured samples. However, their small volume prevents us from detecting any magnetic signal. We focus then on the well-defined 'large' LSMO nanoislands. Indeed, such nanoislands can be well discerned against the non-magnetic background, mainly because of their edge contrast. On one hand, the edges of abrupt features are the places where the feedbacks fail and thus they are also the places that most likely show the convolution of different interactions. On the other hand, we cannot completely rule out the magnetic nature of that intense contrast: first, the contrast remains identical under changes of the scanning direction, suggesting that it could be a real effect, not an artifact from the tip-island edge interaction (Fig. 4.6). Second, the geometry of the island, faceted in the (111) planes, also favors such contrast. As shown in the sketch of Fig. 4.5, the magnetization always tends to align with the structure edges, in order to minimize the magnetostatic energy. It may thus be reasonable to have such intense dark contrast in the nanoisland edges when the out-of-plane applied field is parallel to the tip magnetization. Finally, one may also notice the darkest spots in the center of some nanoislands (inside black squares in Fig. 4.6). Although hard to distinguish, they indicate an out-of-plane magnetization direction, parallel to the tip magnetization. This result could indicate the nanoislands show a vortex configuration, with in-plane magnetic moments except in the center or vortex core, where the magnetization points out-of-plane. We shall discuss this configuration later in the Chapter.

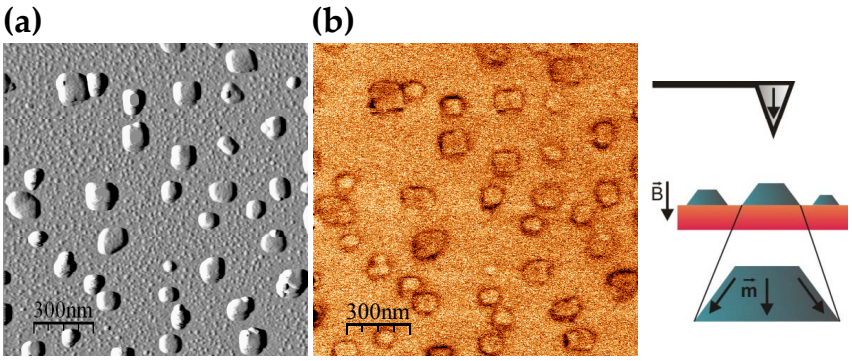

Fig. 4.5: *(a) Amplitude image of the LSMO nanoislands showing the faceted morphology of their truncated pyramid shape. (b) Corresponding MFM image acquired while applying 30 mT to the sample. The main dark contrast is located at the edges. A sketch of the tip and sample magnetic moments is displayed on the right hand side.*

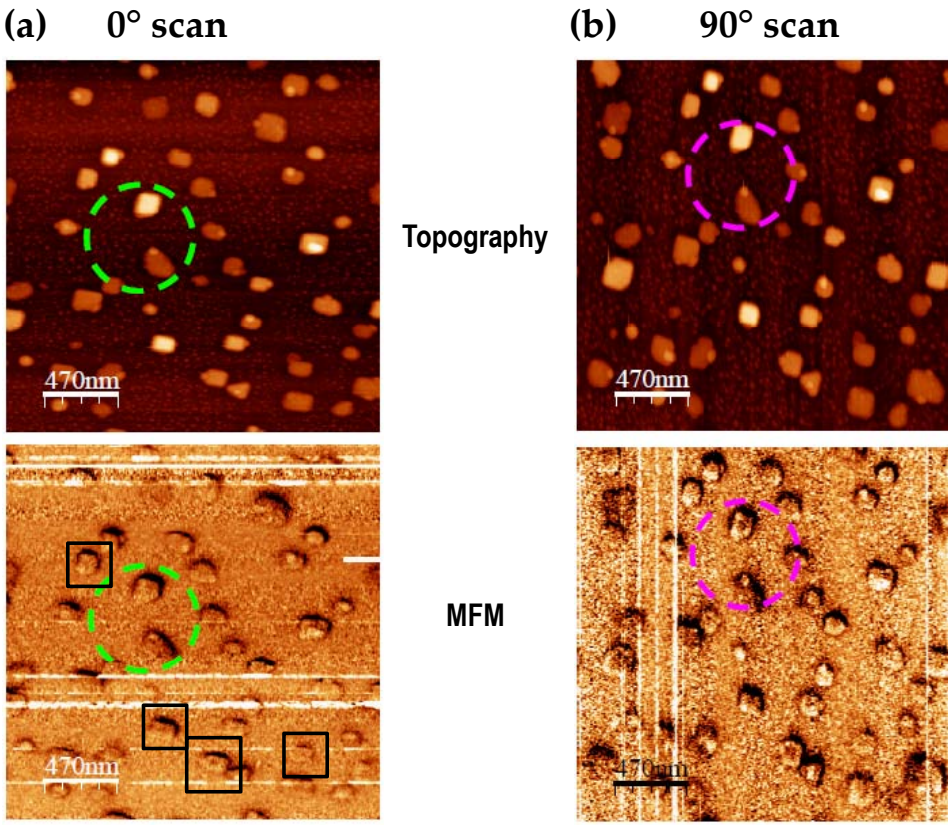

Fig. 4.6: *(a) 0° and (b) 90° scanning of the self-assembled LSMO nanoislands with applied out-of-plane magnetic field. The dark contrast on the island edges is more intense at one of the island sides. This is presumably caused by a certain inclination of the cantilever and hence of the tip with respect to the island. Such inclination induces the island walls to interact differently with the two-side coating of the tip (which is a point dipole only in a simplistic approximation). The fact that the darkest side remains the same during the two scans reveals the magnetic nature of this contrast. If it were an artifact, the dark side would change together with the scanning direction.*

From the faint contrast we have seen above, it seems clear that the magnetic interaction between the tip and the islands is too low to enable further analysis. By using a tip with higher magnetic moment the contrast should in principle increase, despite also risking to influence the sample magnetic structure with the tip. Fig. 4.7 displays the resulting magnetic contrast using a tip of higher magnetic moment under 30 mT, in remanence, and under -20 mT out-of-plane applied field. When the 30 mT are applied parallel to the tip magnetic moment, some of the edge-contrast seen before is still present but now we may also see a blurry dark contrast, typical of magnetic contrast, throughout the entire island. This contrast fades a little in the remanence image [Fig. 4.7(b)], and seems even weaker when the field is applied in the opposite direction to the tip [-20 mT, Fig. 4.7(c)]. The change in the contrast is better seen in the line scans of an individual island [Fig. 4.7 (d)]. This behavior accounts for the magnetic nature of the islands: the larger dark contrast is seen when the magnetic moment of the island is parallel to that of the tip (attractive interaction); into the surface, in this case. By decreasing the field and changing its orientation, we expect the island to switch into an 'out-of-the-surface' magnetization. However, the field applied is not strong enough to achieve the reversal of $\vec{m}$, otherwise we would see the bright contrast characteristic of the repulsive interaction. These results apparently contradict what we deduce from the SQUID magnetization loops of Chapter 3: according to them, 20 mT should be enough to saturate the island out-of-plane, which we do not see with MFM. Seemingly, under the influence of the stray-field of the tip, the effective field sensed by the nanoisland is less than 20 mT: i.e. the field, applied opposite to the stray field, only decreases the magnitude of the attractive interaction but it does not achieve the magnetization reversal. Therefore, although we have gained in sensitivity, the influence of the tip modifies our nanoislands and thus precludes the study of their spontaneous magnetic structure.

Assessing the optimal magnetic tip

The above experiments underline the critical role of the magnetic tip and illustrate some of the tests done using both commercial magnetic and in-house sputtered Si tips. Among the tips tested, the commercial tips from Nanosensors proved to be the most appropriate for our samples, and will be used in the following experiments. Their relevant parameters are listed in Tab. 4.1. The majority of the tips used in MFM are Si-based tips coated with magnetic layers that are tens of nm thick. The higher the magnetic moment of the material or the thicker the coating, the larger the tip magnetic sensitivity will be. On the other hand, as we already mentioned, the high stray field caused by a highly magnetic tip may modify the original domain pattern of the sample. Also, for thick coatings, the large tip radius may decrease the resolution. An exhaustive study of the characteristics of a large number of magnetic tips is reported in [231]. The only difference between the two tips used from now on is the thickness of the coating , which is made of a CoCr alloy (see Tab. 4.1). This means that the thinnest coated tips have a lower magnetic moment (LM) and a smaller radius (see Fig. 4.8).

According to what we said in section 4.1, non-destructive MFM imaging implies that the magnetic sample and tip should fulfill Eqs. 4.8 and 4.9, where the parameters involved are the tip and sample saturation magnetizations M_S and anisotropy fields H_K. In Chapter 3 we presented the SQUID values for the saturation magnetization and coercive field (H_C) of our system of LSMO nanoislands grown on YSZ. For room temperature in the in-plane

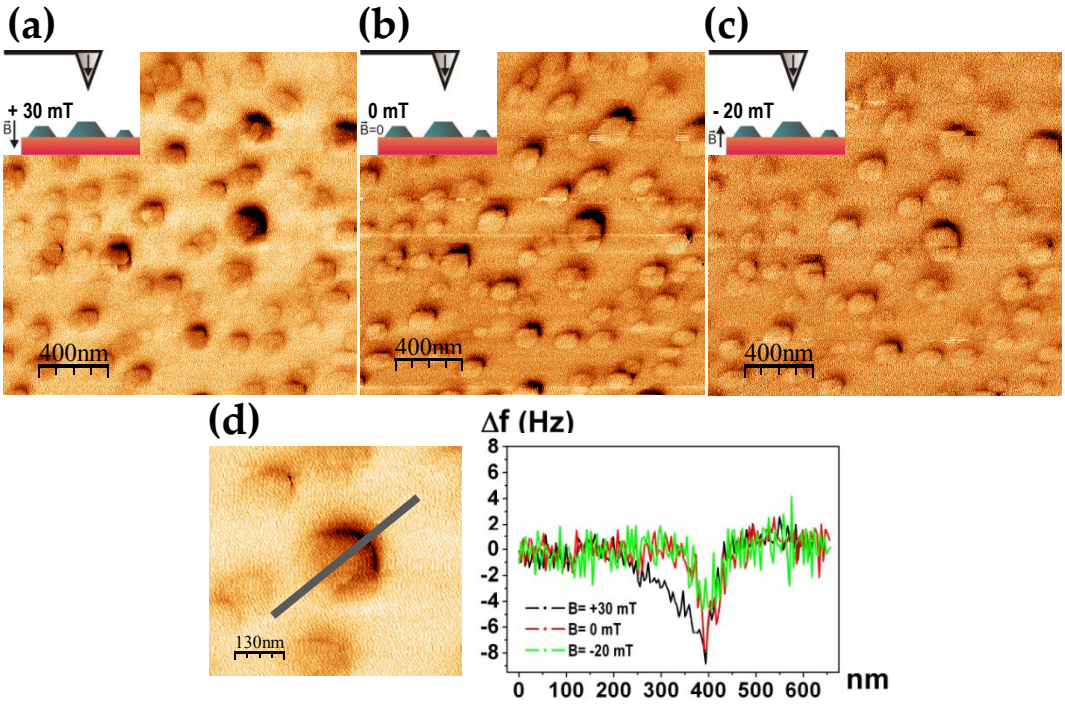

Fig. 4.7: *MFM images of LSMO nanoislands using a high magnetic moment tip under 30 mT (a), 0 mT (b) and -20 mT (c) out-of-plane magnetic field. (d) Zoomed image of a single nanoisland and its corresponding MFM contrast line scan under the different applied fields.*

Tab. 4.1: *Technical parameters of the two tip models utilized.*

Tip	f_0 (Hz)	k (N/m)	Radius (nm)	Coating (nm)	H_c^{th} (Oe)	H_c^{exp} (Oe)	$\lvert\vec{M_S}\rvert$ (emu/cm^3)
1.	75	2.8	$\lesssim$30	20	250	280	150
2.	75	2.8	$\lesssim$50	40	350	380	300

Data are from [233] except for H_c^{exp}, which is deduced experimentally. Tip 1 stands for PPP-LM-MFMR tip, known as the low-moment (LM) tip, and Tip 2 is the standard PPP-MFMR tip. The given H_c^{th} and saturation magnetization M_S values are from measurements on a flat surface. In contrast, H_c^{exp} is the result of the real tip-end characterization obtained from measuring a magnetic hard disc with in-situ *applied field [231].*

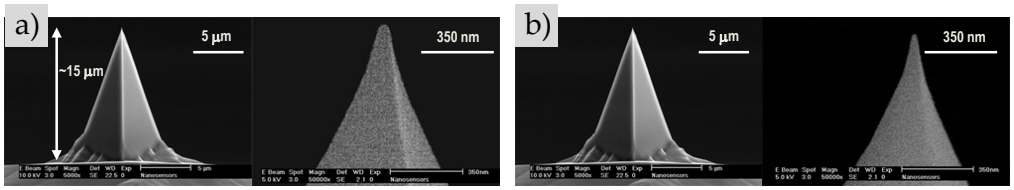

Fig. 4.8: *Scanning Electron Microscopy micrographs of the employed Nanosensors MFM commercial tips. (a) PPP-MFMR tip. Full front view of the tip (left) and zoom of the tip-end with radius∼50 nm (right). (b) PPP-LM-MFMR tip. Full front view of the tip (left) and zoom of the tip-end with radius∼30 nm (right). From [233].*

configuration, the estimated M_S was 300±40 emu/cm^3, and the coercive field value H_C ∼20 Oe, for nanoislands grown from 0.03 M precursor solutions (see Tab. 3.3). The latter is a large value compared to soft magnetic materials like Iron (1 Oe) and Permalloy (0.05 Oe for $Fe_{21.5}Ni_{78.5}$) [234], but very low compared to hard materials like Alnico V (640 Oe) [234], Cr-Co-Pt hard disk drives (1700 Oe) [235], or Nd-Fe-B alloys (10,000 Oe) [236]. It is also considerably smaller than the coercive fields of our CoCr-coated tips [280 Oe (22.3 kA/m) for low moment LM Tip 1 and 380 Oe (30.2 kA/m) for Tip 2]. We can deduce the anisotropy fields of the sample from the in-plane and out-of-plane hysteresis cycles of Chapter 3, which give a value of around ∼4225 Oe (∼336 kA/m). For the anisotropy field of the tip we may take the value of the coercive field, since its hard-ferromagnet cycle is reasonably squared. Regarding the saturation magnetization values, instead of them we take the remanence magnetization values of tip and sample: it seems more appropriate in this case, since we initially look at the tip-sample interaction in remanence. For the tip, in any case, the remanence magnetization equals the saturation magnetization value, because of its hard-magnet square hysteresis loop. For the sample, in contrast, the measured remanence magnetization is far lower than the saturation value: we take the value measured with SQUID for the system of self-assembled LSMO nanoislands, i.e. 61 kA/m. Consequently:

$$\text{From Eq. 4.8 } \frac{H_K^{samp}}{M_{rem}^{tip}} \geq 1 \Longrightarrow \begin{array}{lrcl} \text{Tip 1:} & 336\ \frac{kA}{m} & > & 150\ \frac{kA}{m} \\ \text{Tip 2:} & 336\ \frac{kA}{m} & > & 300\ \frac{kA}{m}; \end{array}$$

$$\text{From Eq. 4.9 } \frac{H_K^{tip}}{M_{rem}^{samp}} \geq 1 \Longrightarrow \begin{array}{lrcl} \text{Tip 1:} & 22.3\ \frac{kA}{m} & \not> & 61\ \frac{kA}{m} \\ \text{Tip 2:} & 30.2\ \frac{kA}{m} & \not> & 61\ \frac{kA}{m} \end{array}$$

From the above lines we may see that both tips fulfill the first condition and neither the second. Thus, in principle, the tip is not expected to modify the sample while, conversely, we could expect the sample to modify the tip magnetic structure. In either case, however, the compared values are quite close to each other and, very importantly, those of the sample are values averaged over a large amount of different nanoislands featuring a variety of sizes and aspect ratios. Therefore, the real anisotropy field and magnetization values of the sample will vary from island to island and the tip to sample interaction will change accordingly. Tip modifications are also to be taken into account: the loss or roughening of the magnetic coating and changes in the tip geometry are quite common during the scanning process. In summary, this simple estimation indicates that the chosen tips are in the range of the appropriate values but also that we will have to look critically at the specific measurements we do in order to discard any possible artifacts.

Given the analysis presented above, it is useful to assess the performance of the chosen tips in some representative measurements, to ascertain that the aforementioned potential artifacts are under control. Fig. 4.9 displays the magnetic force micrographs of the LSMO nanoislands grown on YSZ (Sample 1) using Tip 1 in (a) remanence, and (b) & (c), after applying opposite in-plane magnetic fields of 21 mT. Image (a) is, as expected, identical to the one shown in Fig. 4.5: islands are mainly identified by their edge-contrast; the contrast within the island is otherwise difficult to detect. We need to apply as much as 21 mT in order to be able to distinguish the white and dark contrasts within each island, which are the signature of a saturated island, i.e. of a single magnetic domain. The contrast is reversed for oppositely applied field, as expected, proving that it is not an artifact due to tip-sample interaction. On the contrary, tip-sample interaction is very weak, as evidenced in the small remanence magnetic signal in (a) and by the fact that we were not able to detect intermediate stages between the remanence and saturation regimes. As expected, there is no influence of the tip on the magnetization of the sample. However, we cannot fully rule out the converse effect. Especially after a long scanning time, it is possible that the sample stray field may influence the tip magnetization. This would go in the direction of reducing the effective tip $|\vec{m}_z|$, with a corresponding decrease in the tip-sample interaction strength. The line scan of a single island in (d) quantitatively shows the variations of the magnetic contrast. Such differences are small, yet clear. The magnitude of the magnetic contrast is also very modest, with a frequency variation no larger than 3-4 Hz, which is not far from the background noise.

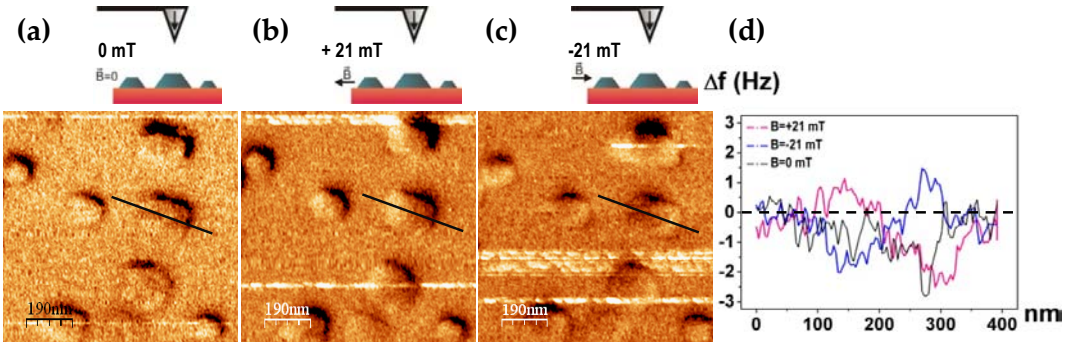

Fig. 4.9: *MFM images of LSMO nanoislands taken with a low-moment tip (Tip 1) in remanence (a) and after saturating the sample by applying in-plane 21 mT (b) and -21 mT (c) fields. The contrast within the islands, unnoticeable in (a), arises as a left to right bright-dark (b), and dark-bright (c), contrast characteristic of saturated single domains. (d) Magnetic contrast profile of an individual island at the different magnetization states shown in (a), (b) and (c).*

Fig. 4.10 shows the topography and magnetic images of Sample 1, as in Fig. 4.9 but now scanned using Tip 2. These images were done after saturating the tip and the sample in opposite directions by applying *ex-situ* an out-of-plane magnetic field of 500 mT. In contrast to the previous case, the use of the thicker-coated Tip 2 yields a very clear magnetic contrast at the nanoisland locations already in remanence. Furthermore, we found no evidence of tip changes caused by the stray field of the islands, which could happen due to the low anisotropy field of the tip (as stated previously in the application of Eq. 4.9). Successive scans of the same area with different scan directions always led to the same island contrasts (not shown), confirming that the tip remained unchanged. The color scale in the MFM image shows a frequency shift range of around 10 Hz, after having appropriately re-

stricted the scale. This is not much larger than the 3-4 Hz range we saw before. However it does make a clear difference. As a matter of fact, it allows us to clearly resolve the magnetic structures of the nanoislands, which have, until now, remained hidden. A close inspection of the image reveals that such different magnetic structures can actually be grouped into three categories, which we name *low contrast*, *vortex state* and *multidomain*, as we will explain in the following. The next section is precisely devoted to the description and analysis of these magnetic structures.

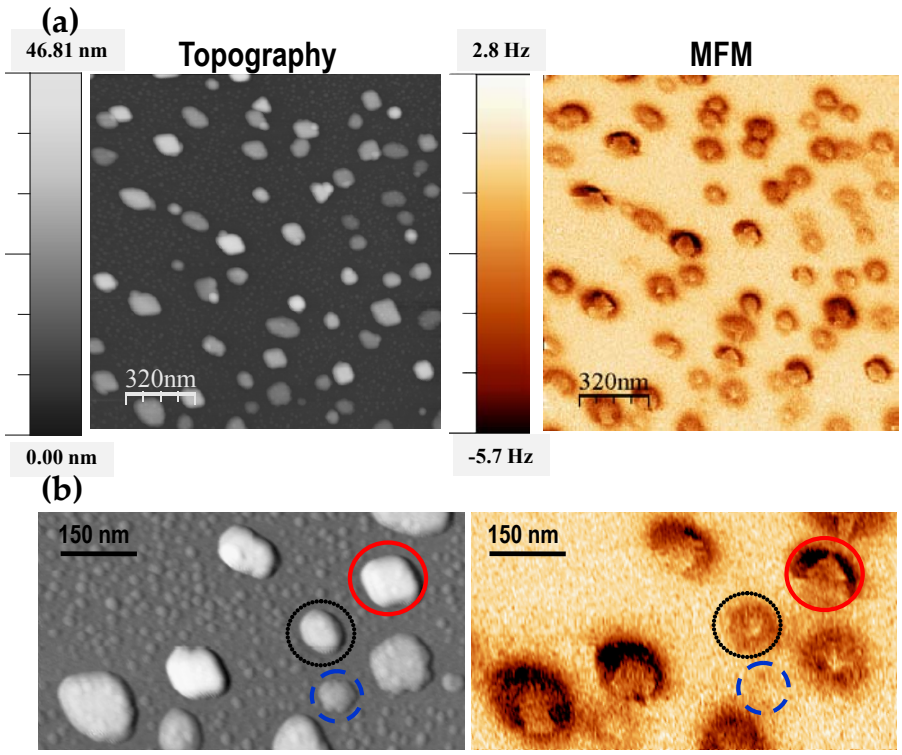

Fig. 4.10: *(a) Topographic and magnetic images of LSMO nanoislands, taken with Tip 2 after having saturated,* ex-situ, *tip and sample in opposite directions. The retrace distance for the MFM scanning was 30 nm. Images were recorded in remanence and at room temperature. The color scale in the MFM image is restricted to comprise only the majority of the values shown by the nanoislands. (b) Detailed topographic and magnetic images of a smaller region with LSMO nanoislands. The dashed (blue) line, dotted (black) line and solid (red) line circles highlight nanoislands with low-contrast, vortex and multidomain magnetic configurations, respectively.*

4.3 Unveiling the magnetic configuration of self-assembled LSMO nanoislands

4.3.1 Nanoisland shape-Magnetic structure correlation

Three different magnetic structures, named *low-contrast* islands, *vortex*, and *multidomain* configurations have emerged from the imaging of LSMO samples with Tip 2 (see previous section). These magnetic structures are, in fact, not randomly linked to the various islands,

but appear correlated to the island size and morphology. We can use the average lateral size D and thickness t of the islands to calculate the average section S_a of every nanoisland configuration. The smaller islands (S_a~0.75×10^3 nm^2), are those exhibiting *low-contrast*, and their domain structure cannot be determined due to the small interaction with the magnetic tip. The medium size nanostructures (S_a~1.33×10^3 nm^2) typically present in-plane anisotropy with *vortex state*, showing the characteristic out-of-plane magnetic contrast in the center of the nanoisland, the so-called vortex core. Finally, the larger structures (S_a~2.50×10^3 nm^2) present *multidomain* magnetic configuration. The existence of not only in-plane but also out-of-plane components of the magnetic moment in these larger islands is in agreement with the macroscopic hysteresis loops measured in the out-of-plane configuration. These, although small, still show remanence magnetization and non negligible coercive field values. It should also be noted that no correlation between the states of adjacent islands was observed. This fact suggests that the interaction between neighboring islands may be disregarded and that they can be treated as independent objects.

Fig. 4.11 shows an example of how the size and geometry of nanoislands determines their magnetic structure. In (a), a medium size nanoisland (D~90 nm, t~30 nm) displays a *vortex* configuration, with the out-of-plane core in the middle. The topography and magnetic contrast line profiles are shown below the image. Conversely, the island in (b), with a similar lateral size but with a smaller thickness, does not give a measurable magnetic signal: this is what we understand by *low-contrast*.

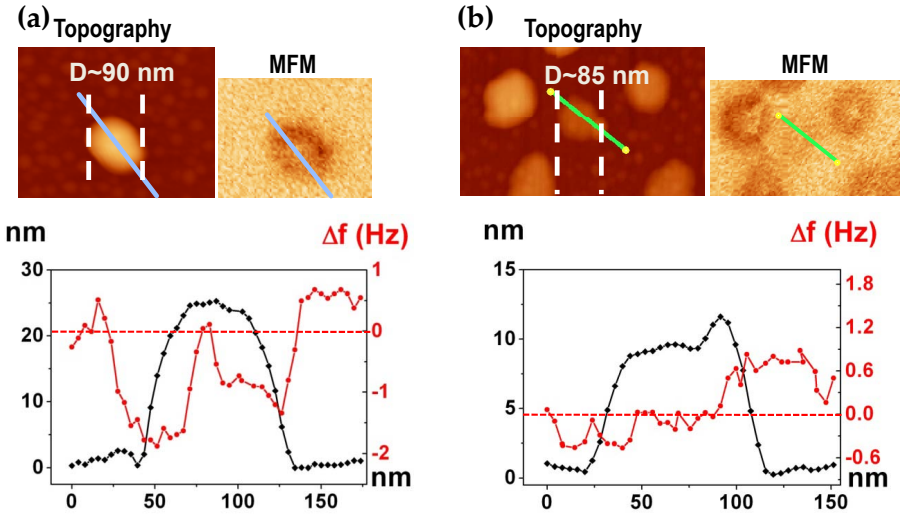

Fig. 4.11: *(a) Topography and MFM images of one LSMO nanoisland and its corresponding line scan across the vortex core. (b) The same as in (a) but for an island with similar width but less than half thick. This island represents the so-called low contrast nanoislands.*

Statistical processing of several areas of about $2\ \mu m \times 2\ \mu m$ results in three distinct regimes, as shown in Fig. 4.12 (a). The magnetic configuration of the islands depends on their lateral size D and thickness t. Although the spread in geometries and shapes is considerable, each of the three magnetic structures appears well confined to certain regions of this map. The larger nanoislands display a *multidomain* configuration and the smallest present a low contrast that seemingly corresponds to a *single domain* state with homogeneous in-plane magnetization. In between, we find the *vortex* state, displaying an out-of-

plane central core, and which we will discuss soon. These three configurations are clearly seen in graph (b), where the histogram shows how many islands of a given volume present each of the three magnetic configurations. The same is done in Fig. 4.12 (c), using the aspect ratio D/t of the islands. At a first glance, the D and t-defined distinct regions from (a) suggest that the aspect ratio may be the determining factor leading to one magnetic structure or the other. However, it follows from the graph in (c) that both multidomain and vortex configurations show similar aspect ratios. This suggests that island volume is eventually deciding between the two configurations.

The *low-contrast* nanoislands, which we assume to be single domains, are at the limit of detection with our experimental set-up. To be able to estimate the interaction between the tip and these small islands, we first assume a dead layer of thickness ∼2 nm (recall the discussion regarding the presence of a magnetic dead layer in Chapter 3). The ferromagnetic section of the low-contrast islands would then have a thickness of about 8 nm (the average thickness for these islands is ∼12 nm). Such nanoislands can be divided into individual ∼8 nm diameter spherical elements that interact with the MFM tip. The force gradient between each element and the tip, separated z∼30 nm, is then about 4.8×10^{-5} N/m *. The total magnetic interaction between the Co coated MFM tip and a LSMO island can be estimated as the sum of the interactions between each element and the Co tip: considering the typical island lateral size to be around ∼80 nm in the case of the small islands, this gives a total value of $\sim4.8\times10^{-4}$ N/m. Meanwhile, the noise of the MFM signal, evaluated as the signal fluctuation when the tip lies away from the islands, is around $\sim4\times10^{-5}$ N/m. Hence, our estimation is around an order of magnitude above the noise limit. Nevertheless, the average experimental contrast that we measure for the *low-contrast* islands is around $\sim8\times10^{-5}$ N/m, only a factor 2 higher than the background noise, which is the reason why it is hardly detected. The estimated theoretical value, $\sim4.8\times10^{-4}$ N/m, nearly an order of magnitude larger than the experimental, thus sets an upper limit for the magnetic signal between the tip and the low-contrast small nanoisland. The discrepancy between the theoretical estimation and the experimental signal may be due to various facts. First, during the experiments, especially under ambient conditions, the tip is most probably oxidized, which increases the effective tip-to-sample distance. Second, because of the scanning process, the magnetic coating might have worn out slightly, decreasing its magnetic moment. Third, an important decrease from the theoretical value could be also expected in case of in-plane magnetic moments, since the theoretical calculation assumes the moments are out-of-plane. From here, the discrepancy between the theoretical and the experimental value could be taken as an indirect confirmation that the magnetization in the ferromagnetic nanoisland lies indeed in-plane. Anyhow, this diversity in the magnetic configuration cannot be inferred from the SQUID hysteresis loops. In such macroscopic measurements the size-dependent magnetic behaviors all add up and reflect the average magnetic characteristics of the nanoisland ensemble.

It is well known that the geometrical constraints determine up to a great extent the magnetic configuration of small structures, taking *small* as "of the order of the characteristic magnetic length scale" (e.g. in the order of the magnetic exchange length). The magnetization pattern of nanoelements represents the lowest total energy configuration, which is the

*We have estimated the interaction between a Co coated tip (with a radius of 10 nm and magnetization value of M_S(Co) = 1440 kA/m) and a LSMO nanoisland divided into 8 nm size elements with M_S(LSMO at 300 K) ∼300 kA/m, using the following equation: $\frac{\partial F}{\partial z} = \sum_i \frac{\mu_0 6 m_{tip} m_i}{\pi z^5}$ where m_{tip} and m_i are the magnetic moment of the tip and the magnetic moment of each of the elements of the nanoisland, respectively, and z is the distance between the tip and each nanoelement.

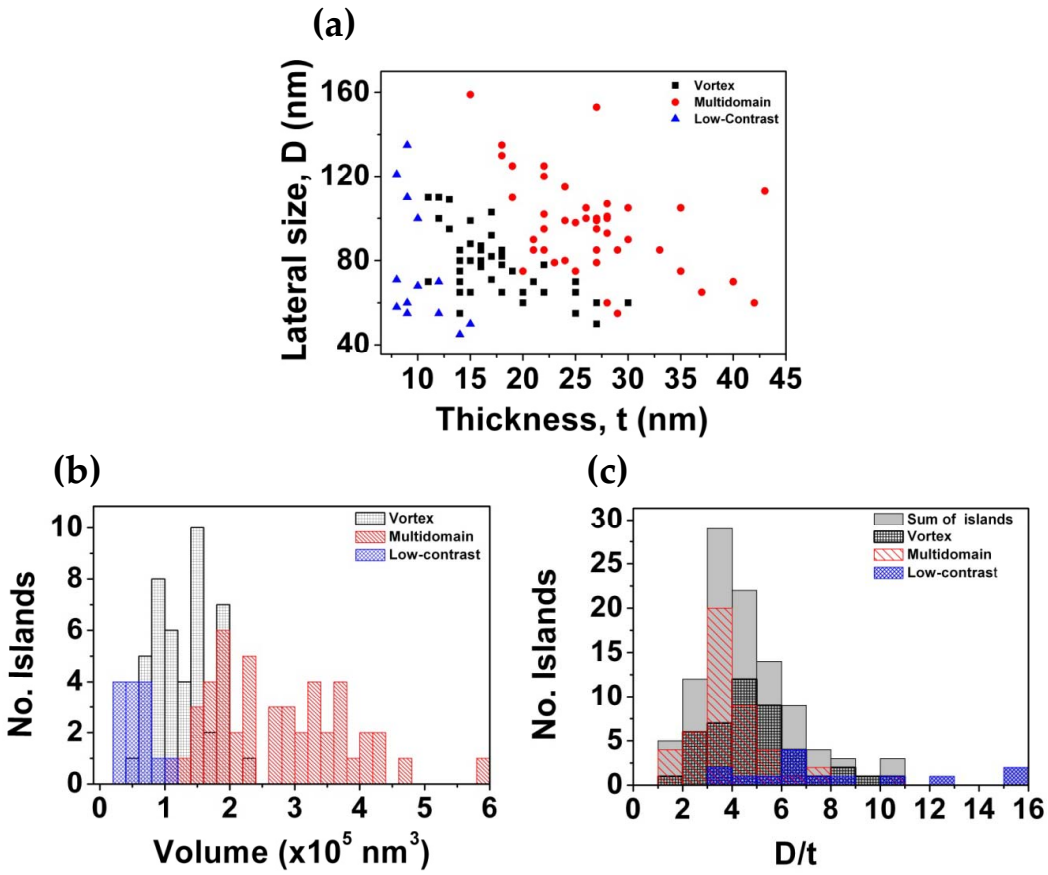

Fig. 4.12: *(a) Magnetic phase diagram extracted from MFM measurements displaying the three magnetic configurations as a function of the nanoisland lateral size* D *and thickness* t. *(b) The volume of the islands against the number of nanoislands, separated in terms of the three possible magnetic configurations. (c) The island population distribution in terms of the aspect ratio* D/t.

compromise among the different competing terms, i.e. exchange energy, magnetostatic or shape energy, magnetoelastic and magnetocrystalline anisotropy energies, and the interaction energy between individual islands. If we consider an isotropic (no preferential crystal orientations for the magnetization) and free-standing magnetic structure (no strain), its magnetic ground state will be uniquely determined by the competition of the *exchange energy*, which tends to align the spins of the atoms, and by the *magnetostatic energy*, which tries to reduce the field in the surrounding space through flux-closure configurations. Below a certain lateral size in the order of 10^{-8}-10^{-11}m, such competition requires that nanostructures display a single domain structure of parallel atomic spins, giving rise to a giant spin [237]. With increasing volume, however, the increase in the magnetostatic energy triggers the particle to break into differently oriented magnetic domains which permit to reduce the stray fields. In between the single-domain and multidomain structures, for particles of a certain aspect ratio, the ground state is the so-called vortex state [10, 38, 44, 238].

The magnetic moments within the vortex curl in-plane, keeping parallel to the side of the nanoelement-in order to reduce the magnetostatic energy- and slowly curve towards the interior of the particle. The large exchange energy around the center gives rise to a singularity known as the vortex core, which exhibits out-of-plane magnetization. The vortex configuration provides a good flux-closure and it is a highly stable magnetic configuration. It may display four different and energetically equivalent magnetic states depending on its *chirality* or *circulation* (the clockwise or counterclockwise sense of the in-plane magnetization) and *polarity* (the outwards or inwards out-of-plane sense of the core magnetization). The hysteresis loops for such a magnetic configuration were first measured in supermalloy ($Ni_{80}Fe_{14}Mo_5$) nanodiscs by Cowburn et al. [38]. The vortex core was later observed in real space by MFM [10], and also with spin polarized scanning tunneling spectroscopy in Fe nanodots [44]. The vortex magnetic configuration has also been measured in submicron patterns defined in LSMO thin films grown by pulsed laser deposition on (001)-$SrTiO_3$ substrates, where the shape of the islands dominates over the crystal field and the epitaxial strain effects to finally determine the domain structure under zero applied magnetic field [66].

In our system of self-assembled LSMO nanoislands we can rule out the magnetoelastic energy contribution because we know from the structural analysis of Chapter 3 that the islands are strain-free. Regarding the magnetostatic interaction between nanoislands, our analysis did not show any correlation between the nanoisland magnetic structure and their spatial distribution, even if some islands sit very close to each other (less than one diameter away). Besides, it is as an extremely challenging task to include an island-island interaction in such a non-uniform distribution of nanostructures; only for regular arrays of elements, such as those obtained from lithography methods, the interaction component could be realistically modeled [239, 240]. Nevertheless, we do need to include the cubic magnetocrystalline anisotropy in the energy expression of our system. This was inferred from the Ferromagnetic Resonance experiments: the in-plane easy axis lies in the <110>$_{LSMO}$ direction, which is the projection of the <111>$_{LSMO}$ magnetocrystalline easy axis. Summarizing the above, the energy of our LSMO nanoislands can be expressed in the following way:

$$E_{total} = E_{exchange} + E_{shape} + E_{magnetocrystalline} \tag{4.10}$$

The above contributions were taken into account in the simulation of the stable magnetization configurations, performed with micromagnetic elements using the OOMMF 3D code [241] by Oscar Iglesias-Freire from the group of Dr. Agustina Asenjo at ICMM-CSIC.

We consider our pyramidal nanoislands as rectangular prisms in a first approximation, and the following LSMO parameters: the magnetocrystalline anisotropy constant K_1 measured in the FMR experiments, the saturation magnetization M_S at 300 K as deduced from hysteresis cycles, and the exchange stiffness A= 1.73$\times 10^{-12}$ J/m taken from the literature [242]. Three different typical islands sizes were evaluated: small (lateral size 50 nm, 10 nm thick), medium-size (lateral size 100 nm, 15 nm thick) and large nanoislands (lateral size 120 nm, 30 nm thick). The obtained results, displayed in Fig. 4.13, reveal what we already saw in the MFM image analysis: the domain configuration depends on nanoisland size. In the case of the smaller islands, we always find a single-domain configuration with in-plane magnetization. Due to the in-plane magnetization of these islands, the MFM contrast (which is proportional to the divergence of the magnetization) is lower than the estimated interaction between the tip and an island magnetized out-of-plane. The majority of the medium-size nanoislands present vortex configuration [Fig. 4.13 (b)] with an out-of-plane component of the magnetization in the center of the island. Finally, the larger islands show a complex magnetization configuration [Fig. 4.13 (c)] with an out-of-plane component of the magnetization in different regions of the island, in agreement with the MFM measurements. It is worth noting how in the vortex-state, where the magnetization is supposedly in-plane except for the core, the magnetic moments exhibit non-zero out-of-plane component (expressed by the presence of red and blue colors throughout the island). A certain out-of-plane component arises in square geometries, due to 90° domain walls that form at the regions where the magnetization vector changes direction. Also, the <111>$_{LSMO}$ easy magnetization axis could contribute to the out-of-plane component of the magnetization. For large islands, the presence of out-of-plane regions gains weight, thus forming domains.

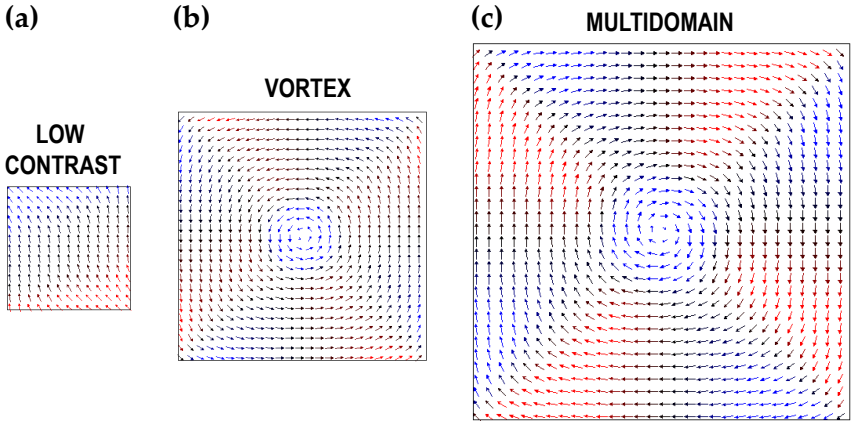

Fig. 4.13: *Results of micromagnetic simulations performed with the OOMMF 3D code. Nanoislands correspond to the following geometries: (a) 50 nm × 50 nm and 10 nm thick, (b) 100 nm × 100 nm and 15 nm thick and (d) 120 nm × 120 nm and 30 nm thick. The data scale for all the simulated images is 25 kA/m. The blue and red colors correspond to the out of plane magnetization (outwards and inwards, respectively). The magnetization configurations were obtained after saturating along the +Z (outwards) direction. Courtesy of O. Iglesias-Freire.*

In conclusion, the MFM results, supported by the above explained micromagnetic simulations, allow for the prediction of the geometries that, in LSMO, yield the single-domain, vortex, and multidomain configurations. The uniform magnetization of single-domain nanoparticles, for instance, is a promising candidate for high density hard disk drive data

storage and magnetoelectronic device applications [243–245]. In turn, the four possible independent vortex states could be used as magnetic bits for data storage. Furthermore, the chirality and polarity control necessary for technological applications has triggered a lot of interest, with recent works reporting the electrical and magnetic switching of the vortex core magnetization and the tuning of the chirality [43, 246–248].

4.3.2 Analysis of the vortex state in sub-200-nm LSMO nanoislands

The analysis shown in the previous section focused on a specific sample that we named *Sample 1* to distinguish it from *Sample 2*, on which we focus in this section. *Sample 2* also displays an homogeneous self-assembly of well-faceted LSMO nanoislands on a YSZ substrate. Note the remarkable number of vortices that can be observed in the $5\ \mu m \times 5\ \mu m$ MFM image of Fig. 4.14. Measurements were done in remanence, after saturating tip and sample in opposite directions. At a first glance, the vast majority of the islands show a bright spot, corresponding to the outwards orientation of the vortex core, although a closer look reveals the presence of some dark spots in the center of some islands (marked with arrows). The predominance of bright spots is due to the prior *ex-situ* saturation, where the islands are first magnetized opposite to the tip (i.e. repulsively interacting with the tip, thus exhibiting bright contrast). When the field is turned off, the island relaxes into the in-plane curling vortex state, with its core pointing preferably outwards.

In addition to the vortex configuration, note that this sample displays a high number of $(111)_{\mathrm{LSMO}}$ oriented nanoislands, crystallized in the form of triangles. Fig. 4.15 shows the MFM forward and backward scan of a group of islands with different magnetic structure. The $(111)_{\mathrm{LSMO}}$ nanoislands exhibit clear magnetic contrast, often the darkest contrast in the image. However, their contrast is influenced by the field of the tip. This is evidenced by the changing of the magnetic pattern with the scanning direction. A reasonable hypothesis is that the tip may trigger a reversible domain wall displacement caused by the small coercive field of the triangles with respect to the tip magnetization.

Unlike the triangular islands, the vortex configuration remains undisturbed during the scanning [see the vortex next to the triangle in Fig. 4.15 (b)]. Note also that, except for the bright core, the vortex state exhibits a dark contrast, characteristic of an attractive tip-island interaction. Recalling that MFM is sensitive to the *out-of-plane* variation of the field generated by the sample, and that the magnetic moments within the vortex are curled *in-plane*, there should not be an appreciable contrast where we actually observe an evident dark contour. There are two issues here to be considered. On one hand, it is not strictly true that no contrast should arise from the region outside the core. The latter indeed holds for perfectly circular structures, where the magnetization swirls continuously within the xy plane. For square geometries, however, a contrast arises at the 90° domain walls of the square diagonals, as commented in relation with micromagnetic simulations of Fig. 4.13. On the other hand, the tip stray field may modify the sample magnetic moments towards the field direction in such a way that the vortex outer region interacts attractively with the tip (dark contrast) [249, 250]. This local modification may happen reversibly, in a way that does not permanently affect the magnetic state of the island. The closer to the sample and the larger the magnetic moment of the tip, the stronger this effect will be. Fig. 4.16 (a) is a simulated MFM image of a permalloy element ($1\ \mu m \times 1\ \mu m \times 10$ nm), where the gray scale represents the contrast to be seen in MFM (proportional to $\vec{\nabla} \cdot \vec{M}$) and the superposed arrows represent the magnetization distribution. Note at how a black (attractive) and a

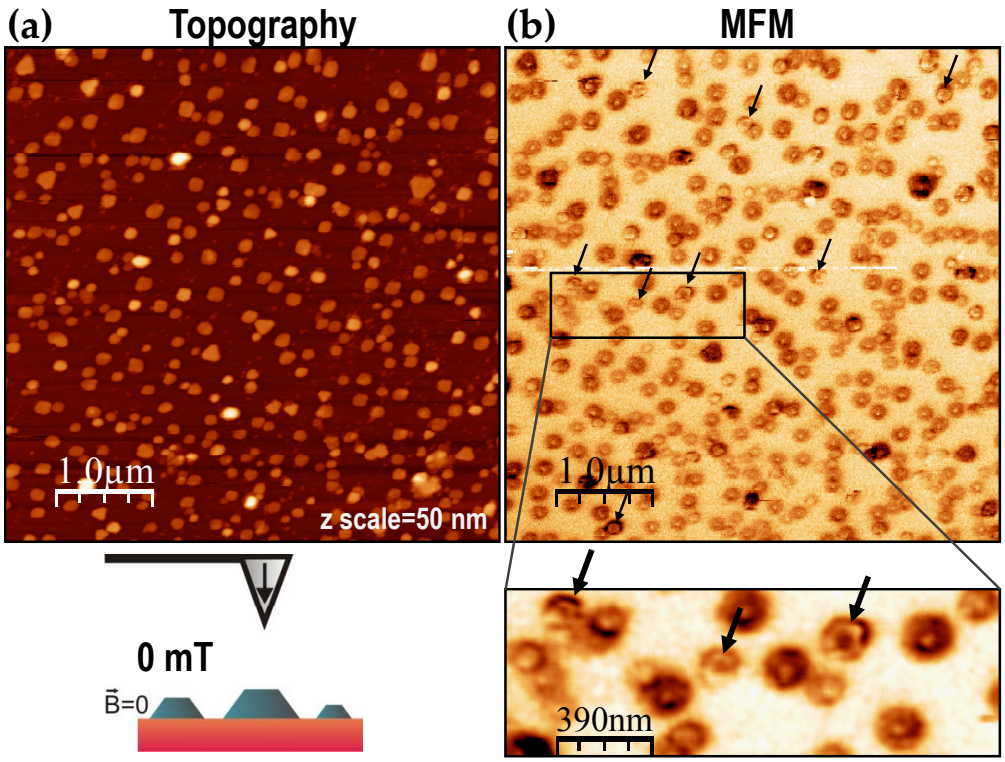

Fig. 4.14: *Topography image (a) and its corresponding MFM image (b) of self-assembled LSMO nanoislands displaying a majority of vortex configuration. Images were taken at zero applied field, after saturating tip and sample in opposite directions. The arrows in (b) mark some of the islands which show dark contrast in the vortex core, namely, inwards magnetization (parallel to the tip). (c) Zoom image from (b). A gaussian filter was applied in order to better distinguish the dark and bright vortex cores.*

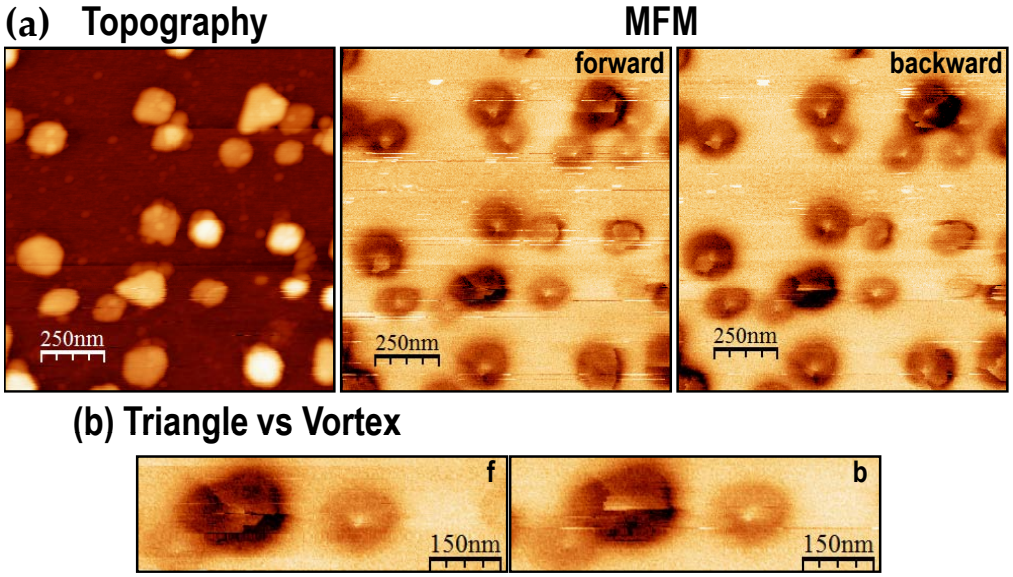

Fig. 4.15: *(a) Topography image (left) and MFM images (center and right), the latter corresponding to the forward and backward scan of the tip. (b) Zoom of a triangular and a square island showing how the magnetic structure of the first varies with the tip scanning direction, as opposed to the vortex configuration, which remains unchanged. Images were taken in remanence, after saturating tip and sample in opposite directions. 'f' and 'b' stand for 'forward' and 'backward' scanning direction, respectively.*

white (repulsive) contrast arise at the four domain walls, different to the gray background where $\vec{M}$ is uniform [228]. In Fig. 4.16 (b) we may see the experimental result of the MFM imaging of such permalloy squares [250]. Fig. 4.16 (c) shows the micromagnetic calculation of a permalloy disk (D=300 nm, t=50 nm). The size of the arrows reflects the magnitude of the in-plane component (from [249]). Image (d) in Fig. 4.16 corresponds to the MFM measurement of a 400 nm diameter permalloy dot exhibiting a bright core (outwards polarization) and a dark outer core region, consequence of the tip-sample interaction (from [250]).

From the above discussion it is reasonable to think that our square LSMO nanoislands may combine both of the effects described. The influence of the tip stray field in orienting the in-plane magnetic moments parallel to the tip would hence add to the contrast due to the domain walls, which, considering the MFM resolution and the small lateral size of our nanoislands [150 nm vs the 1000 nm of Fig. 4.16 (a) and (b)], cannot be as well-defined as in Fig. 4.16 (b).

Regarding the vortex core, some authors have deduced, using analytical and numerical tools, that it grows wider with increasing island thickness. This is a consequence of the relative decrease in magnetostatic energy due to the reduced out-of-plane demagnetization field in thicker elements. The core M_z distribution thus widens to lower the exchange energy[†]. In our results we do not see such a correspondence between the core lateral size and the island thickness t. Fig. 4.17 (a) shows the D vs t diagram of the measured vortex configuration, indicating islands with a *narrow* core $\leq$100 nm (solid dots), and those with a $\geq$100

[†]For instance, the core can display a domain-like $\geq$100 nm-wide central region within 200 nm diameter (0001)-Co circular dots of D/t $\leq$8 aspect ratio [251].

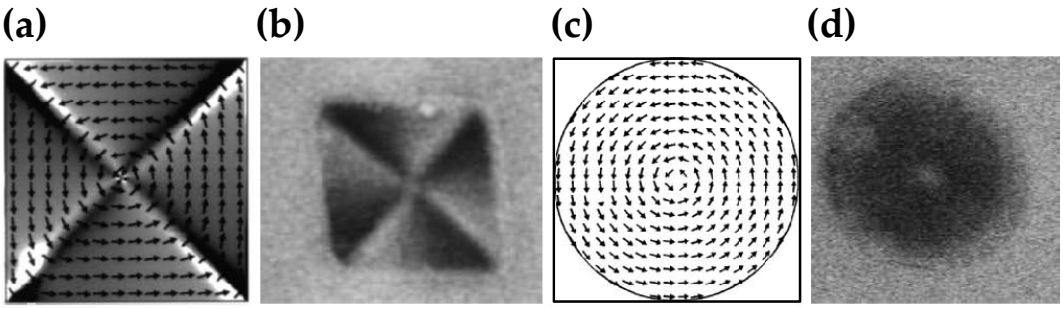

Fig. 4.16: *(a) Calculated magnetization distribution (arrows) and the expected MFM contrast, proportional to* $\vec{\nabla} \cdot \vec{M}$ *(grey-scale) in a 1 μm × 1 μm × 10 nm square permalloy element [228]. (b) Real MFM image of a 1 μm × 1 μm × 50 nm permalloy structure exhibiting the flux-closure structure contrast linked to the presence of domain-walls [250]. (c) Micromagnetic simulation of the magnetization in a D=300 nm and t=50 nm permalloy disk [249]. (d) MFM image of a D=400 nm and t=50 nm disk exhibiting the global attractive tip-sample interaction in the outer region of the vortex. The vortex core is the bright spot in the center of the dot [250].*

nm *wide* core (open dots), which could suggest the concentric-ring structure discussed in reference [251]. Fig. 4.17 (a) evidences that neither *narrow* nor *wide* cores appear related to a higher or a lower aspect ratio region of the diagram. The MFM image in Fig. 4.17 (b) and the corresponding line scans in Fig. 4.17 (c) illustrate what we mean by *narrow* and *wide* cores: their average width w is ∼30 nm and ∼100 nm, respectively. Particularly, these two islands have very similar D and t values yielding aspect ratios in the 9-10 range. The trend described in the literature, hence, is not visible in our MFM results.

A word of caution is in order here regarding the comparison between literature and our experimental results. Theoretical models and experimental studies available in the literature concern different materials and different measuring techniques. The energies involved and the approximations made in them might thus not be applicable to our specific case. For example, the islands reported to show a larger core width with increasing thickness are *hcp* Co cylinders [251], while our LSMO nanoislands are square pyramids with beveled facets, at a 54.7° angle from the substrate surface. The higher the islands, in this case, the smaller the top facet will be. Therefore, it is not evident that the demagnetizing field will decrease in such a geometry, not at least in the manner simulated in reference [251].

An important fact that we have not mentioned yet is that the vortex core sizes deduced from our MFM images are the convolution of the tip-sample interaction, and thus they are likely to be overestimated. Moreover, it appears that the major influence of the tip stray field over the stable vortex configuration is precisely the broadening of the vortex core we discussed above. Fig. 4.18 (a) shows that such broadening is caused by tip-sample interaction, since it varies depending on the scan direction. Such a modification was not detectable in the islands from Fig. 4.17, suggesting that both a real and a tip-induced broadening coexist. The effect of making the vortex core appear wider than it is in reality is a well known issue, intrinsically linked to scanning probe techniques. The tip-sample convolution responsible for the lateral resolution limit is greater in MFM measurements than in topography measurement, due to the *larger* effective tip size: the sample interacts with the stray field of the tip, which is less localized when farther away from the sample surface. From our images we find that the lateral size of the vortex core takes values in the ∼30-

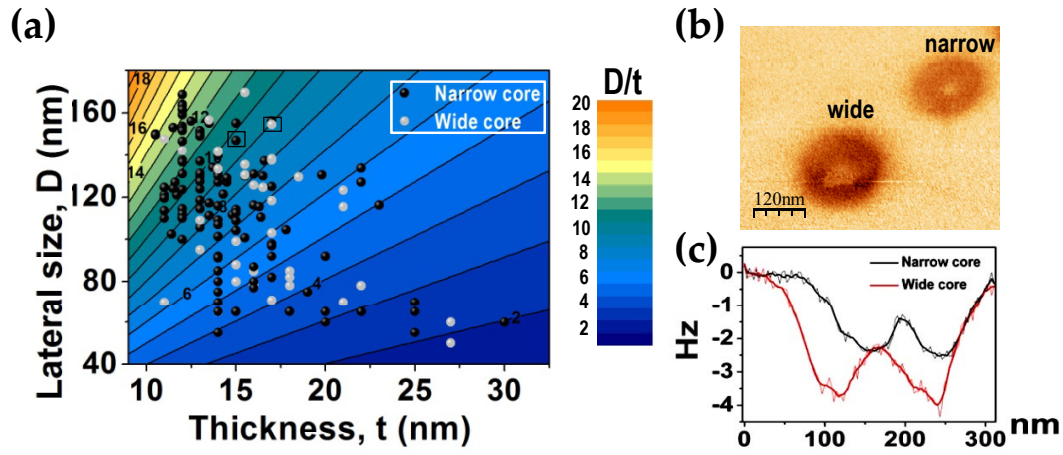

Fig. 4.17: *(a) Diameter* D *and thickness* t *of nanoislands displaying vortex state, separated according to the size of their cores as seen with MFM. Narrow core vortices (solid dots) and wide core vortices (open dots), exhibit core lateral sizes below or above ∼100 nm, respectively. The blue to red color scale expresses ascending* D/t *values. (b) MFM zoom image of two representative islands exhibiting a narrow and a wide vortex core. They correspond to two islands within the 9-10* D/t *range highlighted inside black squares in graph (a). (c) Line profiles across the two vortex cores shown in (b). The lines marked strongest correspond to the smoothing of the real signal, noisier, also drawn. The values measured are ∼40 nm (narrow core) and ∼100 nm (wide core).*

150 nm range. Values in the literature are also in this range for permalloy [10, 249, 250] or Nickel [248] nanostructures observed by MFM. Improvements to MFM measurements have made it possible to achieve 15 nm and even 10 nm lateral size resolution, although measuring at very low temperatures (5.2 K) [252]. To go beyond these limit requires the use of other techniques. An estimation of the real vortex core diameter w of soft ferromagnetic (FM) materials, in the thin-film limit, can be obtained by comparing the exchange and the magnetostatic energies (the two main contributions that dominate the vortex formation).

$$w_{t\to 0} = 2\sqrt{A/K_d} \tag{4.11}$$

where A is the *exchange stiffness* and $K_d = \mu_0 M_S^2/2$ [44]. Using a value of A=1.73×10^{-12}J/m for the exchange stiffness of LSMO [242] and M_S(300 K)= 300 kA/m, as calculated from SQUID, $w_{t\to 0}$ ∼11 nm. In their 2002 work, Wachowiak and co-workers showed the first experimental evidence of a 9±1 nm size vortex core in Fe islands achieved using spin-polarized scanning tunneling microscopy (SP-STM), which is reasonably close to the 6.4 nm value obtained from the theoretical estimate [44].

The vortex core dimension can also be derived from the analytical description of the magnetization distribution within the core. Following the recent work by Mejía-López and co-workers, one can replace the discrete distribution of magnetic moments with a continuous $\vec{M}(\vec{r})$ distribution.The vortex core profile is then described by the z component of $\vec{M}(\vec{r})$, i.e. $M_z(\rho)$, where $\rho = \sqrt{x^2+y^2}$ [253]:

$$M_z(\rho) = M_S\{1 - \frac{\rho^2}{l_{ex}^2}[1.83 + 1.35(\frac{t}{l_{ex}})^{0.4}]^{-2}\}^4 \tag{4.12}$$

In the above expression, M_S is the saturation magnetization, l_{ex} is the *exchange length* and t is the dot thickness. The exchange length l_{ex}=5.5 nm was calculated from $l_{ex} = \sqrt{\frac{2A}{\mu_0 M_S^2}}$

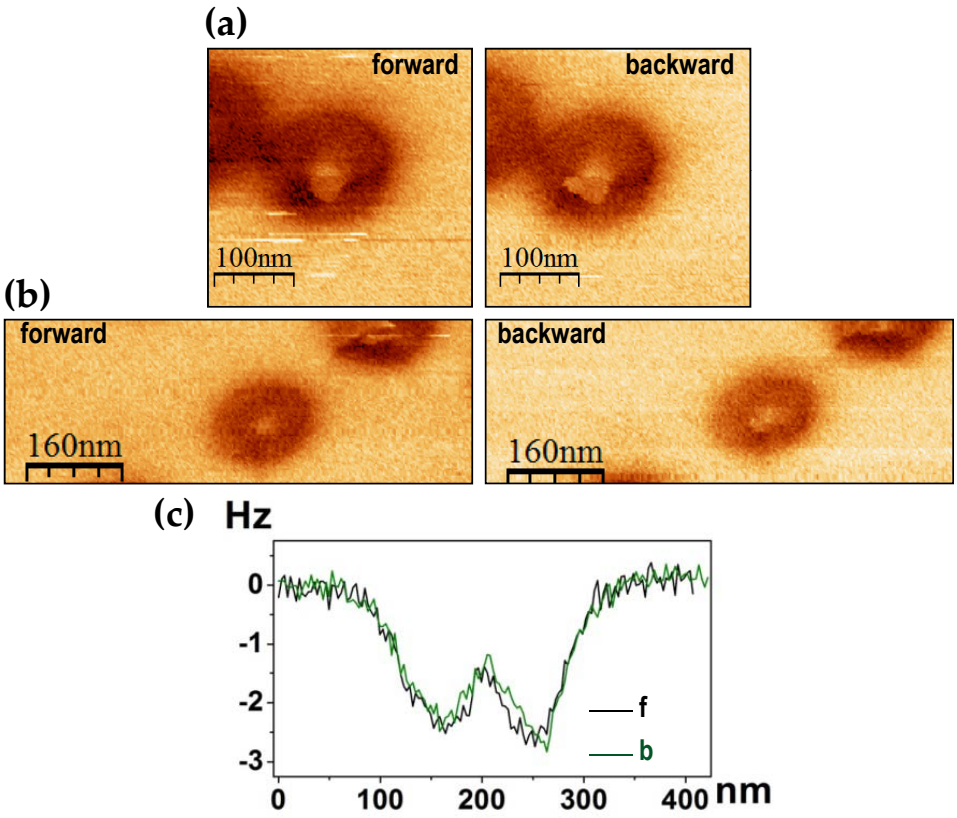

Fig. 4.18: *(a) Forward and backward scan MFM images of a zoomed vortex structure. The bright contrast arising from the out-of-plane core appears somewhat diffuse and its appearance changes with the scan direction, indicating the influence of the tip. (b) Forward and backward MFM scans showing a vortex structure. The definition of the core is slightly worse in the backward scan and thus appears slightly wider. (c) Line scans along the vortex cores of (b). In agreement with the observation in (b), the vortex core is a bit wider during the backward scan. The core appears to be ∼80 nm in diameter. The calculated diameter is ∼11 nm at 300 K (see text).*

[51, 254] where M_S(300 K)=300 kA/m, A the exchange stiffness of LSMO [242]. Eq. 4.12 is derived for non-interacting cylindrical polycrystalline dots, after minimizing the total energy consisting solely of the magnetostatic and exchange contributions (i.e. neglecting the magnetocrystalline anisotropy). Note that the core distribution is independent of the lateral size of the island. It is also assumed that the core shape does not depend on the z coordinate. Fig. 4.19 (a) shows the 3D spatial distribution of the normalized M_z component of the core, according to Eq. 4.12, for the particular case of our LSMO t=20 nm high islands. We have plotted the projection of the 3D graph on the OXZ quadrant, for various t values, in Fig. 4.19 (b). The vortex core lateral size is approximately the full width at half maximum (FWHM) value [253], which leads to w∼2×6.5=13 nm for the t=20 nm case. The larger the nanoisland thickness t, the wider the core will be, and vice versa, in agreement with the previously discussed reference [251]. Fig. 4.19 (c) shows the linear increase of the core lateral size w with t, for the particular range of thicknesses displayed by LSMO nanoislands. In the thin film limit, the linear fit gives w∼10 nm, which is in very good agreement with the vortex core size as calculated from Eq. 4.11. It follows from here that the theoretical core width values lie well below our MFM experimental resolution

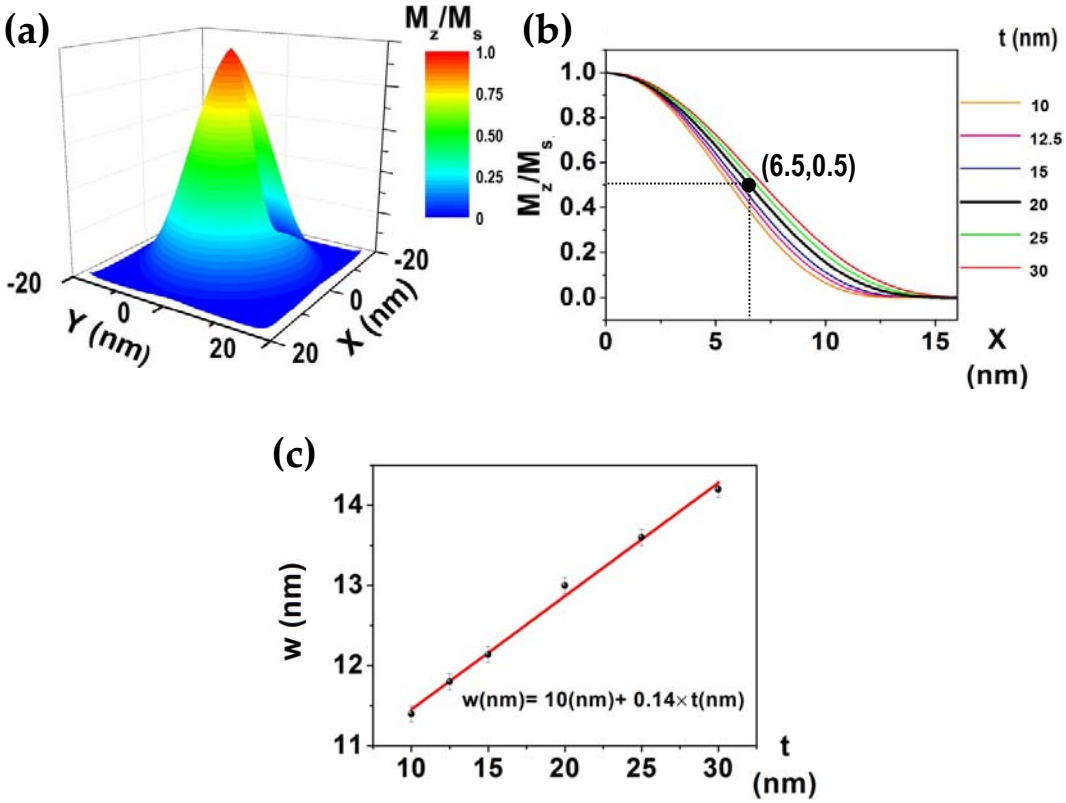

Fig. 4.19: *(a) 3D plot of the M_z spatial distribution within the vortex core, according to the Eq. 4.12 derived by Mejía-López et al. [253]. We took island thickness* t = 20 *nm. (b) Projection of the graph in (a) on the OXZ quadrant. The M_z distribution is calculated for the different set of* t *values shown by LSMO nanoislands. The vortex core width* w *is taken at the FWHM value. Variation of M_z (c) Vortex core width* w *plotted against the nanoisland thickness* t*, extracted from graph (b). At the thin film limit (*t ∼*0)* w *approaches 10 nm.*

Integration of Eq. 4.12 over the whole island volume yields the total magnetization

produced by the vortex core. This calculation provides an upper limit in our case, since the expression from reference [253] assumes cylindrical shape. Fig. 4.20 (a) shows that the magnetization within the core constitutes a sizable fraction of the total M_S in the case of nanoislands with small D, and rapidly decreases for larger diameters. Note that for thicker islands the core magnetization is slightly larger. This latter tendency is illustrated in Fig. 4.20 (b) for different lateral sizes. We can deduce from there that the variation of M_z with thickness is small for the particular thickness range we are interested in. Only for the case of very small diameters (D=40-50 nm) does M_z show an appreciable increase.

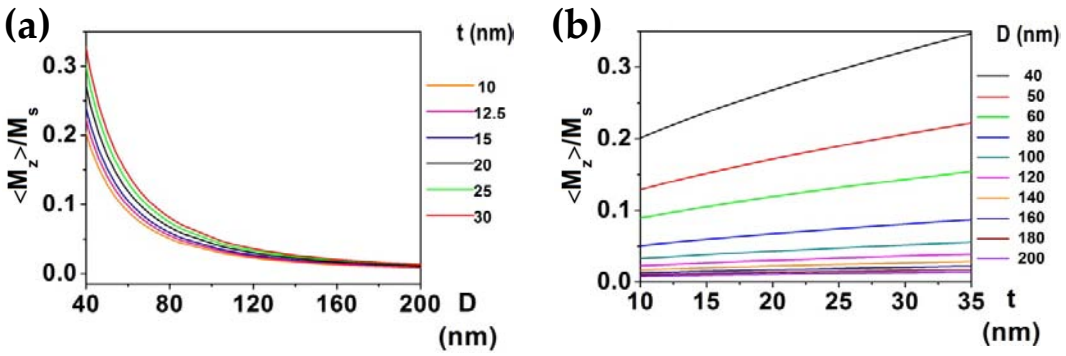

Fig. 4.20: *(a) The total M_z produced by the vortex core within the island rapidly decreases for increasing island lateral size. (b) Evolution of normalized $\langle M_z \rangle$ with nanoisland thickness. $\langle M_z \rangle / M_S$ varies very little with* t *except for the narrowest islands with* D $\leq$*60 nm.*

4.3.3 Completing the magnetic structure landscape in sub-200-nm LSMO nanoislands

In addition to the contrast-changing triangles and the vortex state, we may identify two more magnetic structures in *Sample 2*: i) some very small islands with low-contrast and ii) other high square-pyramid islands with an undefined contrast, exhibiting alternate bright and dark areas that sometimes depend on the scanning direction. We can identify the latter with a multidomain configuration. The different appearance with respect to the previously discussed *Sample 1* multidomain islands may stem from their slightly different morphology: in *Sample 2* they show larger thickness values and lower aspect ratios. A representative example of both i) and ii) islands is marked inside colored squares in Fig. 4.21 (a). The graph in (b) shows the sample aspect ratio distribution as a function of the magnetic configuration of more than a hundred islands. This graph is equivalent to the Fig. 4.12 (c) graph obtained from the statistical processing of *Sample 1*, except that the present additionally features $(111)_{\mathrm{LSMO}}$ oriented nanoislands. Note also that the multidomain islands appear in this case limited to low aspect ratio values [Fig. 4.12 (c)], which explains why they exhibit a rather different contrast from the multidomain islands observed in *Sample 1*. In fact, the cubic magnetocrystalline anisotropy of the system, with the $< 111 >_{\mathrm{LSMO}}$ easy directions [82, 255], could be playing a key role here: since the trend towards in-plane magnetization is weakened for low D/t values, the magnetocrystalline anisotropy contribution, which pulls the magnetic moments parallel to the $< 111 >_{\mathrm{LSMO}}$ directions, would be favored, resulting in the magnetic configuration that we observe.

Vortex states are mainly observed in soft ferromagnetic polycrystalline nanoelements

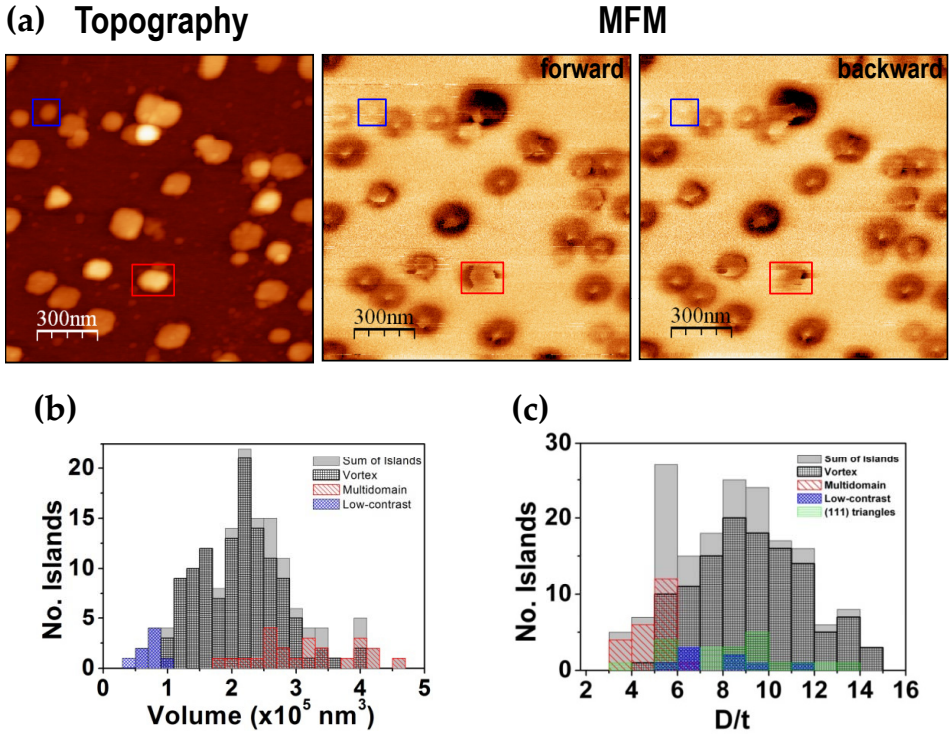

Fig. 4.21: *(a) 1.5μm $\times$ 1.5μm topography and MFM images of a LSMO nanoisland ensemble. Examples of each a small low-contrast island (blue square) and a high changing-contrast island (green square) are given. (b) The volume of the islands against the number of nanoislands, separated in terms of their possible magnetic configurations as seen by MFM (triangles not included). The large volume nanoislands (in red) we have named multidomain. (c) D/t aspect ratio distribution of the nanoislands separated in terms of their magnetic structure. While the vortex configuration is the most easily stabilized, those showing the largest volume (named multidomain) exhibit the lowest D/t values.*

sometimes called platelets because of their high D/t values, often above 10 [256–258]. It is worth noting that LSMO nanoislands display vortex configuration also at D/t values as low as 4. A very recent work has proposed that a beveled geometry of the nanoislands, obtained by cutting their edges away, promotes vortex nucleation in permalloy submicrometre disks. This is explained in terms of a symmetry breaking introduced by the beveled edges, which lowers the energy barrier for vortex nucleation within a saturated single domain state [258]. Fig. 4.22 (a) collects the results from the MFM analysis of the two types of LSMO/YSZ samples measured. Full dots stand for *Sample 1* and open dots for *Sample 2*. A symbol of the same color and shape represents the same magnetic configuration. The plot illustrates the consistency of the observed magnetic structures, leading to a complete magnetic phase diagram of the solution-derived LSMO nanostructures. Note that *Sample 2* exhibits thinner and wider nanoislands in general, in addition to the $(111)_{\mathrm{LSMO}}$ oriented triangular nanoislands islands (in green). We have plotted the latter only to illustrate their usual sizes, because they have different crystallographic orientation and hence they are not expected to comply with the tendency shown by the rest of the nanoislands.

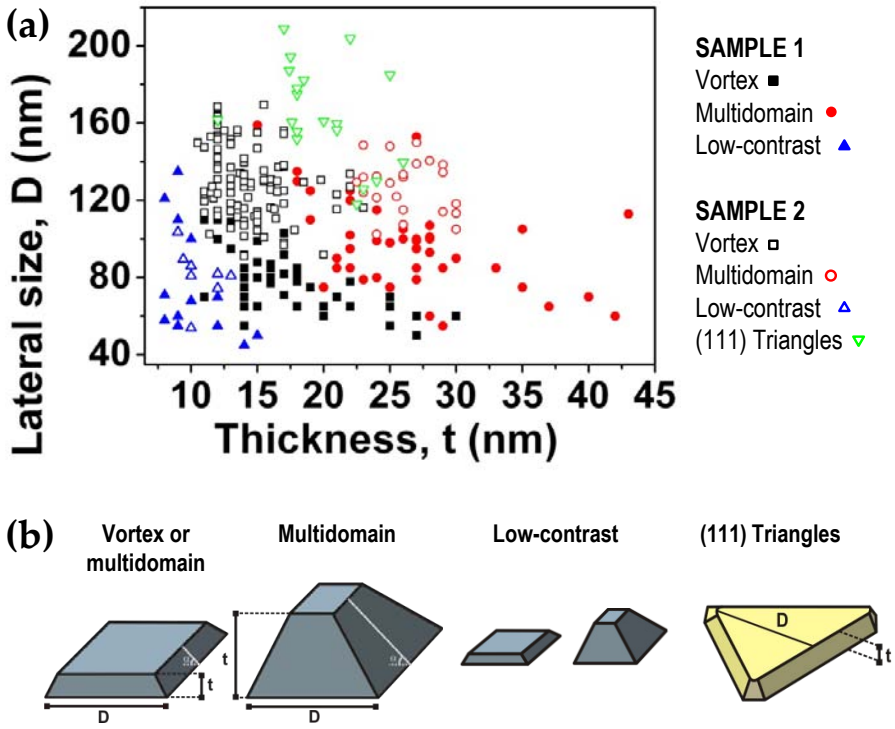

Fig. 4.22: *(a) Magnetic phase diagram relating the nanoisland magnetic structure and its shape. Both the contributions of nanostructures from* Sample 1 *and* Sample 2 *were taken into account. Except for a certain ambiguity in large and high islands showing either vortex or multidomain configuration, the magnetic structure of the vast majority of nanoislands is defined by its shape. Triangles are included for the sake of completitude. (b) Sketched geometries of the nanoislands displaying the different nanomagnetic behaviors.*

In order to further investigate the effect of increasing island thickness on the magnetic structure of nanoislands, mentioned before, we discuss here one last example, where nanoislands were grown onto a Zr-doped Cerium Oxide (CZO) buffer layer (∼20 nm thick-

ness) on YSZ. The LSMO on CZO/YSZ system is equivalent to the LSMO on YSZ system, in terms of LSMO island morphology and their crystallographic orientation, except that they tend to display larger thickness values. Note that Cerium Oxide displays a fluorite structure, the same as YSZ. The great majority of the LSMO islands grown on top of the CZO buffer layer of Fig. 4.23 have heights above 50 nm and aspect ratios in the D/t∼3-4 range. Both the MFM forward and backward scan images are shown, giving evidence that the magnetic contrast does not vary too much with the scanning direction (except for the (111) triangular island, where the contrast varies, as in the previous cases). The majority of islands are, once more, square-base pyramids, but we observe no vortex states for these specific geometries. Fig. 4.23 (c) is the same graph as in Fig. 4.22, but now including the data from a few dozens of LSMO islands on a CZO buffer layer. From the MFM images it is not straightforward to determine the magnetic configuration, although the different shades within each island suggest a multidomain structure (not fully resolved due to the limited resolution). Further micromagnetic simulations, taking into account the real shape of the island, would be required to shed some light on the specific magnetic structure of these islands.

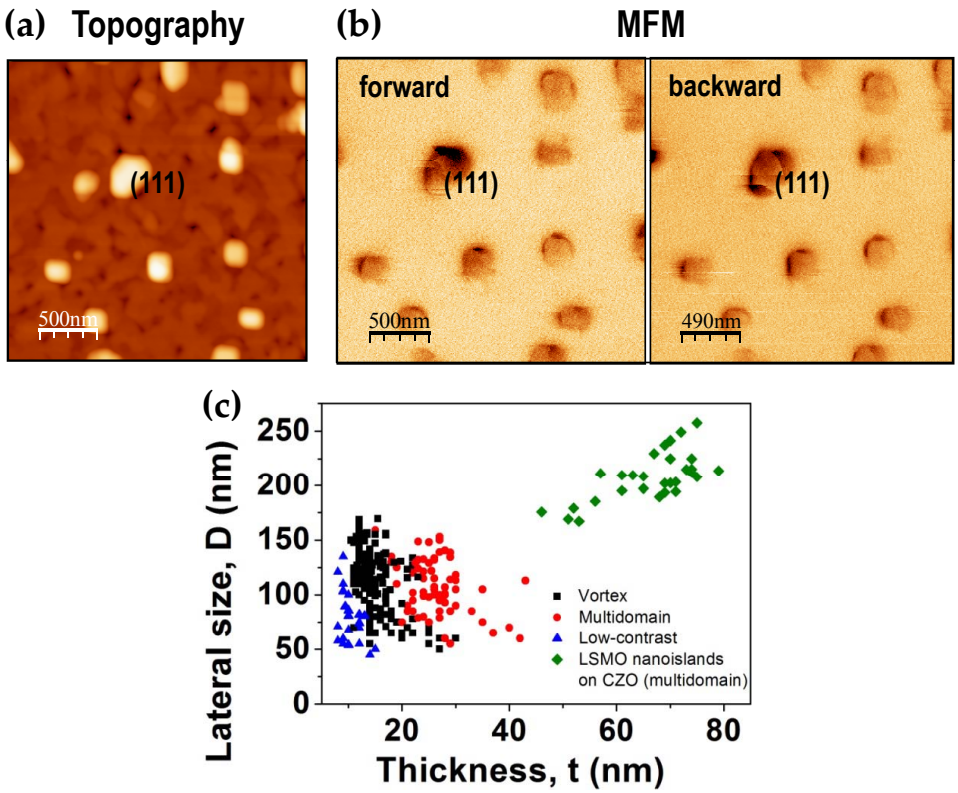

Fig. 4.23: *(a) Topography and (b) MFM images of LSMO nanoislands grown on CZO buffer layer. (c) Graph from Fig. 4.22, included the* D − t *correlation of LSMO nanoislands grown on top of a CZO buffer layer.*

4.4 System evolution under applied magnetic field

4.4.1 General considerations

Throughout the previous section we have described the rich variety of magnetic structures adopted by solution-derived LSMO nanoislands. In particular, we showed that the vortex-state is the preferred configuration for a broad range of LSMO nano-sized geometries. It is now of great interest to study the field stability of these LSMO vortices and, more generally, the behavior of LSMO nanoislands under applied magnetic field. The magnetization reversal process in ferromagnetic nanoelements is very important, not only from a fundamental perspective but also from a technological point of view. The implementation of magnetic nanostructures in modern applications requires knowing, for instance, under what fields the configuration is stable and when it switches magnetization. These processes are governed by the competing energies listed in Eq. 4.10, to which we must now add the Zeeman contribution due to the presence of an external applied field:

$$E_{total} = E_{exchange} + E_{shape} + E_{magnetocrystalline} + E_{Zeeman} \tag{4.13}$$

We could deduce, from the imaging of our LSMO nanoislands, that the vortex configuration is very stable, as proved by successive scans with a relatively high-moment magnetic tip. In their 2002 paper, Shinjo and co-workers revealed the stability of magnetic vortices subject to *out-of-plane* applied magnetic fields [259]: the application of 0.25 T in the direction opposite to previously saturated vortex cores left the core magnetization of circular permalloy dots unaffected. Raising the field up to 0.35 T reversed the magnetization of only the 24% of the cores. Their measurements for constant thickness dots of different aspect ratios (D/t=4, 8 and 20) showed that the necessary field to switch the vortex core, $\sim$0.4 T, did not depend on the lateral size of the dot, further proving that the core is an independent entity within the surrounding in-plane magnetic structure (recall what we commented regarding the expression for its magnetization, Eq. 4.12).

By contrast, the evolution of the vortex state under *in-plane* magnetic field offers wider possibilities with much smaller fields involved. It is well known that the magnetization reversal in such a case proceeds via vortex nucleation, displacement, and annihilation [38, 260]. The new ground state is no longer the centered vortex state but a new state, now stabilized by the Zeeman contribution (Eq. 4.13). Fig. 4.24 illustrates how the vortex state evolves under in-plane magnetic field, both for a cylindrical (a) and a square (b) prism: the domain with the magnetic moments parallel to the applied field grows at the expense of the rest while trying to keep a flux-closure configuration. The core of the vortex is hence gradually pushed to the edge of the element, where it is annihilated, and a saturated single domain state is reached. The left panel of Fig. 4.24 (a) shows the canonical hysteresis cycle of a vortex, adapted from [260], for a permalloy cylindrical nanodot with D=200 nm and t=30 nm: the saturated state (A) is followed by the vortex nucleation (B), where a sudden loss of magnetization occurs until the dot adopts the centered-vortex ground state at zero applied field (C). Under increasing opposite field, the core moves in order to minimize the Zeeman term (D) i.e., in the direction determined by its chirality. Finally, the vortex is annihilated, under fields typically in the thousands of Oersted range [38, 260], yielding the saturated single domain state (E).

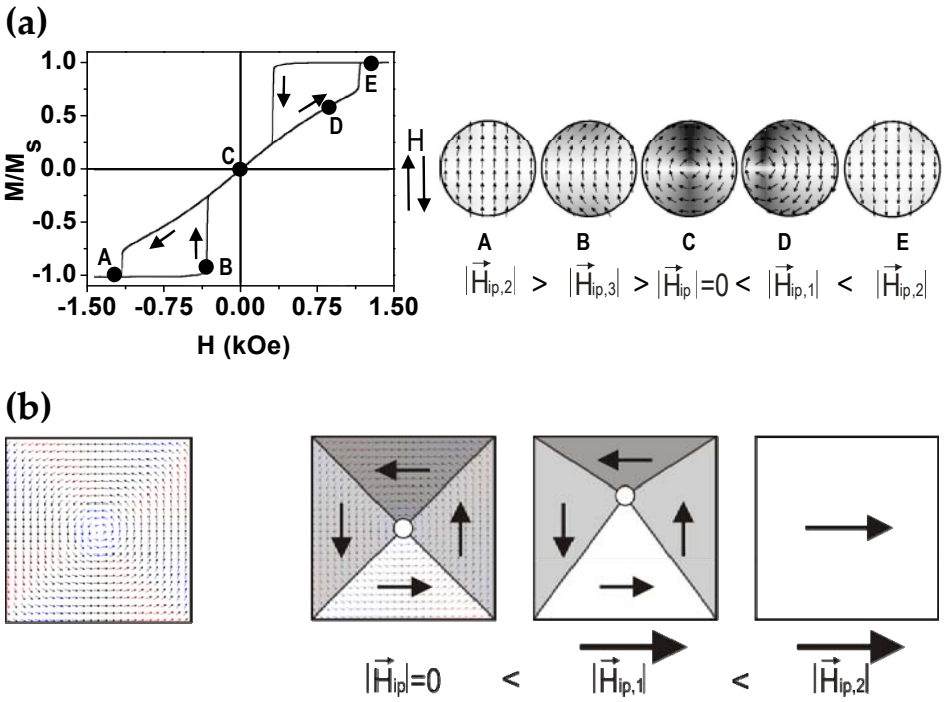

Fig. 4.24: *(a) Typical hysteresis loop showing the vortex nucleation, displacement, and annihilation process and the simulated magnetization reversal in a D=200 nm and t=30 nm isolated permalloy dot (adapted from [260]). (b) Simulated vortex configuration for a LSMO square 3D dot, with D=100 nm and t=15 nm (left panel). The vortex structure is simplified in terms of the four main domains and the central core within the square geometry (right panel, left). Under in-plane applied field, the vortex core displaces and finally disappears. These steps would correspond to stages (C), (D) and (E) in the magnetization loop (a).*

4.4.2 Experimental results

Fig. 4.25 (b) shows the MFM images of a group of LSMO nanoislands in remanence, and under opposite in plane magnetic fields [(c) and (d)]. The amplitude image in Fig. 4.25 (a) recalls the topography shape of the islands, and a black triangle on the left side of every picture serves as reference, since successive scans cause the tip to shift from its original position due to thermal drift. The remanence image was taken in the usual manner, i.e. after saturating tip and sample *ex-situ* in opposite directions. We were able to apply a maximum *in-plane* field of ∼450 Oe. Note that the general shift of the bright vortex cores is in the direction of the applied field.

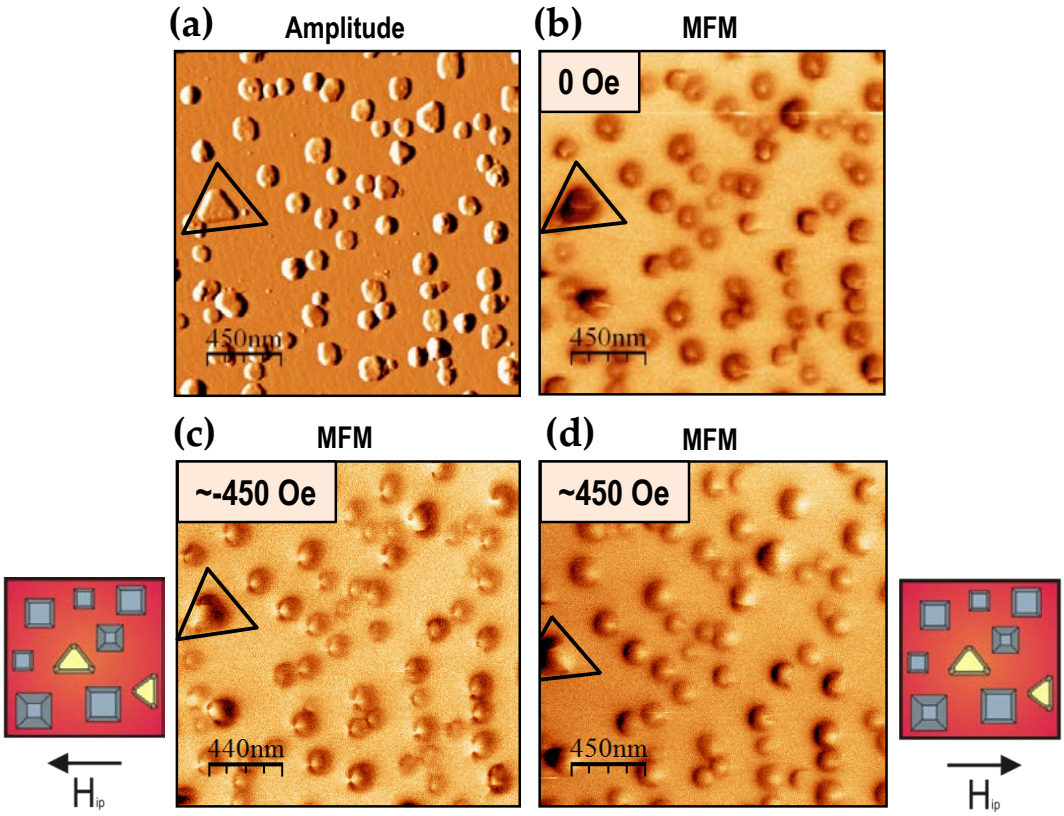

Fig. 4.25: *(a) Amplitude image of Sample 2 LSMO nanoislands showing their faceted geometries. (b) MFM image of the same region taken in remanence. Note the presence of different magnetic structures, previously described, including a large number of vortices. (c)&(d) MFM images of the same region under ∼450 Oe external field applied parallel to the substrate edge. The sketches at each side of the figure illustrate the direction of the in-plane magnetic field. A large triangular nanoisland is marked in every image for reference.*

A closer inspection of the magnetic behavior of nanoislands, displayed in Fig. 4.26 confirms the general tendency observed in the low-magnification images of Fig. 4.25. Three regions, labeled *1*, *2*, and *3* are marked with white squares in the topography image at the top of the figure. Zoomed-in magnetic contrast images of such regions are displayed below, along with their topography and MFM line scans. A representative example of each of the different magnetic behaviors found in the nanoislands has been analyzed: The **vortex-state** (V) in *Region 1* shows the leftwards and rightwards shift of its core under leftwards and

rightwards applied magnetic field, respectively. The line scan reveals the presence of the bright core at 0 Oe, and a seemingly dipolar bright-dark contrast under 450 Oe, characteristic of a saturated single domain state [248, 257]. Note that the dipolar contrast appears clearer at 450 Oe, whereas at -450 Oe it has a horse-shoe structure. This asymmetry is most likely due to the presence of a remanent field at zero applied current, which causes the effective field in both directions not to be identical. In other words, the values we give of the fields are approximate, and -450 Oe is in practice less in magnitude than 450 Oe, so the latter does not saturate the island. The small island in between the two medium-size islands in *Region 1* is an example of low-contrast island, which are at the limit of sensitivity of our equipment, and which we know from micromagnetic simulations to display a **single-domain** (SD) structure. Indeed, its weak magnetic contrast, less than 1 Hz in magnitude, shows no observable structure change when imaging at different magnetic fields. *Region 2* gathers a series of vortices and also a **triangular** (T) $(111)_{\mathrm{LSMO}}$ island. The remanence image of the triangle may resemble that of a vortex, but we cannot confirm it, since the backward scan is different from the forward scan shown in the image; as we already explained, the stray field of the tip sweeps the domain walls within the triangle back and forth during the scan. In any case, it appears clear that the island reaches saturation for both -450 Oe and 450 Oe, as indicated by the bright-dark dipolar contrast. The fact that the two saturated states show a contrast of similar magnitude (opposite in sign) confirms our belief that these are magnetically *softer* islands. Finally, the high square (SQ) islands in *Region 3*, with the undefined **multidomain** structure, also show a tendency towards a single domain saturated magnetic state under external in-plane field.

Field values below the $\sim$450 Oe yield slightly off-centered vortices, as shown in Fig. 4.27. The intermediate states between -450 Oe and 450 Oe reveal the gradual displacement of the vortex core, from the aforementioned horse-shoe structure to that of the saturated nanoisland. The change in the location of the core apex in the example from *Region 1* changes imperceptibly for fields in between -200 Oe and 200 Oe. This is not unexpected, since the lateral MFM resolution, around 50 nm, does not allow to resolve the exact location of the $\sim$10 nm wide core. Notice, nevertheless, the presence of a dark spot near the bright vortex core. This spot most likely indicates the attractive interaction between the tip and the field distribution within the core. The fact that it shifts position with changing magnetic field is a clear signal that the structure of the core is rearranging under the influence of the field, although we cannot resolve this movement. The island in *Region 2* exhibits the same magnetization reversal process as the island in *Region 1*, although it appears somewhat noisier and the dipolar contrast expected at 450 Oe appears less clear. Furthermore, it would appear that the bright vortex core, although weak, can still be distinguished at 450 Oe. The island in *Region 2* exhibits a lower aspect ratio than the previous *Region 1* island ($\sim$7.7 against $\sim$11), suggesting that, the lower the aspect ratio, the higher is the field required to annihilate the vortex. In the following we will see that this is in agreement with theoretical predictions.

4.4.3 Theoretical analysis

We can compare our experimental observations with the theoretical prediction of vortex evolution under applied field. Guslienko and co-workers have long treated this problem for the case of cylindrical soft FM nanodots, reaching the analytical expressions for the magnetic fields required to nucleate a vortex out of an in-plane saturated state (B_n, nu-

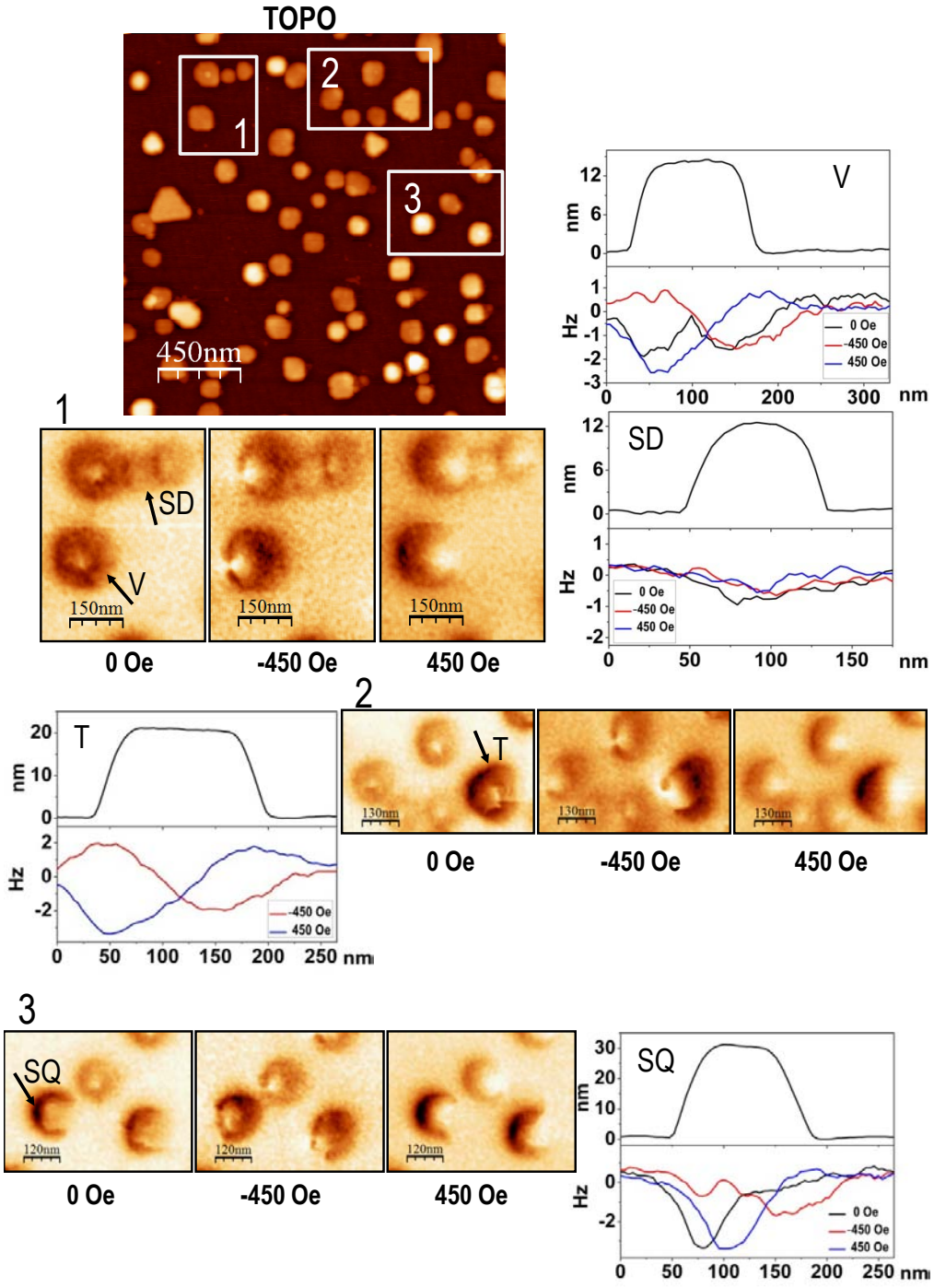

Fig. 4.26: *Topography and MFM analysis of LSMO nanoislands in remanence and under in-plane magnetic field. Three white squares in the upper 1.5μm $\times$ 1.5μm topography image mark the zoomed-in 1, 2, and 3 regions displayed below. Vortex (V) and single domain (SD) structures are shown in Region 1, a triangle (T) appears in Region 2 and the high square multidomain island (SQ) is shown in Region 3. Their corresponding topography and magnetic contrast line scans are displayed on the sides of the MFM images.*

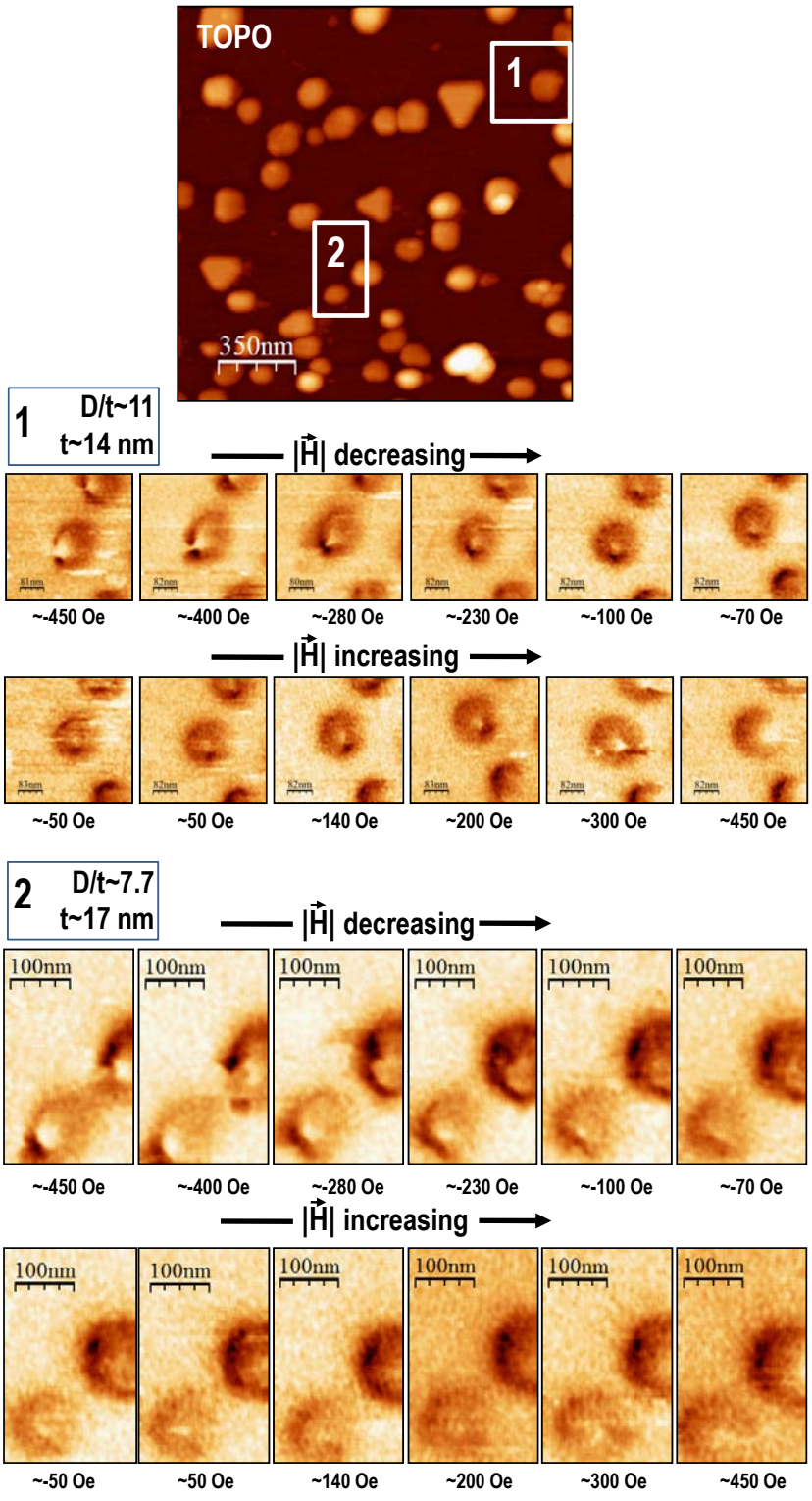

Fig. 4.27: *Evolution of the magnetic contrast of LSMO nanoislands under in-plane magnetic field. The MFM images are zooms from the Regions marked 1 and 2 in the above topography image. Note how the dipolar contrast, characteristic of a saturated island, appears clearly in the island with aspect ratio ∼11 whereas the island in Region 2, with lower aspect ratio, does not exhibit a saturated state.*

cleation field) and for the magnetic fields required to expel the vortex from the dot (B_{an}, annihilation field) [39, 260]. Starting from the remanence state where the vortex core sits at the center of the disk, B_n and B_{an} are calculated by minimizing the total energy of the shifted vortex state with respect to the relative vortex core displacement $s = 2l/D$, with l the displacement of the core and D the dot diameter. The sum of magnetostatic, exchange and Zeeman energy contributions for a given vortex core displacement s then leads to the following analytical expressions of the nucleation and annihilation fields (in Gauss) [39, 260]:

$$B_{an} = 2M_S \left[2\pi F_1(\beta) - \frac{1}{2} \left(\frac{2l_{ex}}{D} \right)^2 \right] \tag{4.14}$$

$$B_n = 4\pi M_S \left[F_1(\beta) - F_2(\beta) - \frac{1}{\pi} \left(\frac{2l_{ex}}{D} \right)^2 \right] \tag{4.15}$$

where $\beta = 2t/D$ and $F_n(\beta) = \int_0^\infty \frac{dx}{x} \left(1 - \frac{1-e^{-\beta x}}{\beta x} \right) J_n^2(x)$, with $n = 1, 2$. $J_1(x)$ and $J_2(x)$ stand for the Bessel function of the first kind and order 1 and 2, respectively. We evaluated the above equations in the t and D range of our LSMO nanoislands and taking the values $M_S(300K)$=300 kA/m and $l_{ex}(300K)$=5.5 nm. The result is plotted in Fig. 4.28, which shows the dependency of annihilation and nucleation field values with respect to the island aspect ratio. According to these graphs, around 120 mT would be required to expel a vortex from a cylindrical polycrystalline LSMO nanodot. This value could go down to 40 mT for the case of an aspect ratio of 10. On the other hand, 40 mT is the greatest value necessary to nucleate a vortex starting from a saturated island, however nucleation values decrease fast when reducing the island thickness t. Both the annihilation and nucleation fields show a similar behavior against D/t, with a sharp increase at very small values and a slower decrease for the great majority of higher D/t-s. For the larger t-s the curve maxima fall below $D/t = 1$ but in the plot only those $D/t \geq 1$ are shown, since in our islands the aspect ratio is always above one. In fact, more realistic expressions for our system would be the ones shown in Fig. 4.29. In the latter, plots from Fig. 4.28 have been confined according to the possible aspect ratio values every island with thickness t can exhibit. This is obtained considering the real D values measured from our AFM studies, i.e., between 40 nm and 180 nm. Tab. 4.2 collects the D/t ranges for each t. The dashed line in Fig. 4.29 (a) represents the maximum field value of 45 mT (450 Oe) we applied in the experiments. This line intersects the set of graphs at a D/t∼7.8, meaning that we should be able to expel the vortex and saturate those islands with aspect ratio above ∼7.8.

Tab. 4.2: *Range of* D/t *values found for a given island thickness* t*, considering that the island lateral size* D *varies between 40 and 180 nm.*

t (nm)		**10**	**15**	**20**	**30**	**40**
D/t	min	4	2.7	2	1.33	1
	max	18	12	9	6	4.5

The above theoretical analysis is useful to understand the evolution of the vortex state under in-plane magnetic field. We must recall, however, that such analysis oversimplifies our system; the real beveled-edge pyramids are approximated as a parallelepiped, and the influence of magnetocrystalline anisotropy is neglected. Hence, its results should be

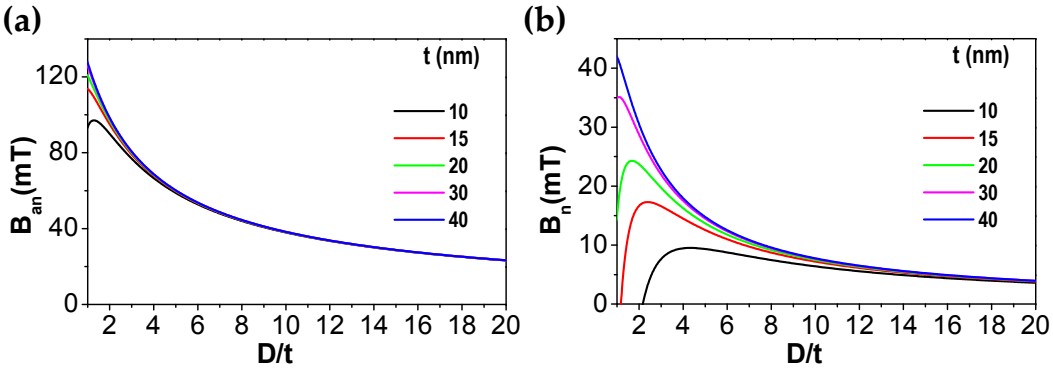

Fig. 4.28: *(a) Vortex annihilation B_{an} and (b) nucleation B_n fields for varying island aspect ratios. The larger* $\mathrm{D/t}$*, the lower the fields required to expel and nucleate a vortex.*

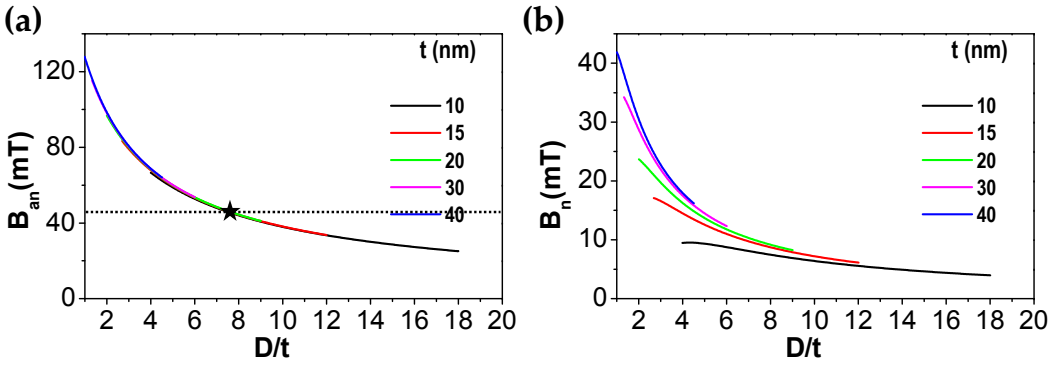

Fig. 4.29: *(a) Vortex annihilation B_{an} and (b) nucleation B_n fields for varying island aspect ratios, restricting the* $\mathrm{D/t}$ *range to the possible values exhibited by the nanoislands, in accordance with Tab. 4.2. The dashed line in (a) represents a field value of 45 mT, which intersects the curves in (a) at* $\mathrm{D/t}\sim$*7.8. Hence, vortex state is to be annihilated in nanoislands with* $\mathrm{D/t}$ *values above 7.8.*

considered qualitatively. Furthermore, these neglected factors could also be influencing the movement of the vortex core, which appears to have a motion parallel to the applied external field, instead of perpendicular to it, as we explained in section 4.4.1 that is the common rule. Indeed, in Figs. 4.25, 4.26, and 4.27 all the observed vortex cores shift parallel to the applied magnetic field. The resolution of the MFM does not permit to resolve with enough accuracy whether the core displacement is perfectly parallel or it exhibits a slightly diagonal shift. However, it is clear that the movement is not perpendicular to the applied field, as it would be expected from the theory (see Fig. 4.24 and related text). The *expected* behavior of the vortex core described there, however, does not consider the role of magnetocrystalline anisotropy. The $< 111 >_{\mathrm{LSMO}}$ easy axis of our LSMO nanoislands, responsible for out-of-plane magnetic moment components in our simulated vortex-state configuration, will certainly affect the domain wall movement, although the way it does so is unclear. The influence of the magnetocrystalline anisotropy could be further reinforced by a small out-of-plane component of the external magnetic field: although the experiment is set up to apply in-plane field, a misalignment, either in the sample position (pasted to the sample-holder) or due to some spatial inhomogeneity in the field, cannot be completely ruled out. Nevertheless, it is unclear how these contributions, other than reducing the efficiency of the parallel field, could produce a 90° orientation change in the core motion.

In addition to the magnetocrystalline anisotropy and to the beveled edges of our nanoislands there are other factors that could be influencing the domain wall motion and hence the core displacement. In our analysis we have always neglected the role of magnetoelastic anisotropy, since the islands appear strain-relaxed. Nevertheless, the presence of strain fields due to misfit dislocations at the island-substrate interface could be affecting the movement of domain walls. Moreover, the likely presence of twin planes due to the fact that the LSMO is not truly a cubic but a rhombohedral structure, could also modify the wall motion [‡].

Very few of the effects listed here, not to say all of them simultaneously, are considered in the vast majority of the reported works on ferromagnetic nanomagnets. As we mentioned in the Introduction of this thesis, the traditionally studied nanomagnets, both experimentally and through simulations, typically refer to regularly spaced polycrystalline prisms. All of the previous factors, unique to our system, plus other possible effects that go beyond our control, make it delicate to derive conclusions on the magnetic behavior of our system. As a consequence, simulations that take into account all of the necessary ingredients are highly desirable in order to get insight into the physical mechanisms leading to our experimental observations.

4.5 Conclusions and outlook

A detailed study of the nanoscale magnetic structure of solution-derived self-assembled LSMO nanoislands has been carried out by means of MFM imaging at room temperature and ambient atmosphere. We have shown that the successful imaging of the system relies on the adequate tuning of the experimental conditions, and, specifically, on the appropriate choice of the magnetic tip. A commercial CoCr coated tip (40 nm thick coating) was found to be the best compromise between sensitivity and sample modification, revealing

[‡] {100} and {110} type twins have been observed in solution-derived LSMO thin films using diffraction contrast TEM [160], p.125.

a clear correlation between the magnetic structure of LSMO nanoislands and their geometrical characteristics. These LSMO nanostructures, featuring lateral sizes D ∼40-180 nm and thicknesses t ∼10-40 nm, exhibit three main magnetic structures, namely, single domain islands, multidomain islands, and islands with a vortex configuration. These configurations are consistent with micromagnetic simulations. From the analysis of more than two hundred islands we have built an experimental magnetic phase diagram showing the geometric stability of each of the magnetic states in remanence. A remarkable tendency towards the vortex-state has been identified in islands with a wide range of aspect ratios $D/t \in$ 5-15, provided that the island thickness was sufficiently small (below ∼20 nm).

In the magnetic vortex state magnetic moments curl in-plane, parallel to the nanoobject edges, in a flux-closure configuration. At the center of the structure, the singularity in the exchange energy is avoided by pulling the magnetization out-of-plane, forming the vortex core. In fact, the observation of the out-of-plane core, represented in most cases by a bright spot at the center of our islands, has been crucial in identifying the vortex state. The small lateral size of the nanoislands (D<200 nm) together with the low resolution (∼50 nm) and the tip-sample interaction issues of the MFM, prevented us from resolving the in-plane domain structure of the vortex. We have further studied the vortex core as a function of the nanoisland D and t, comparing our observations to analytical expressions derived for the expected core width. These give a theoretical value below 15 nm, well below our experimental resolution. Finally, we have analyzed the evolution of our LSMO nanoislands under an in-plane applied magnetic field, reaching values up to ∼45 mT. These have shown the *parallel* motion of the vortex core with respect to the applied field, in contrast to the expected *perpendicular* movement. Using analytical expressions derived for polycrystalline soft cylinders, we have argued that the fields required to nucleate (B_n) and annihilate (B_{an}) a vortex rapidly decrease with increasing aspect ratios. However, application of the existing models must be regarded with caution. First, the vast majority of them are derived for isotropic prism geometries, whereas our LSMO nanoislands exhibit a beveled pyramid shape and a $< 111 >_{\mathrm{LSMO}}$ easy magnetization axis. Second, it is reasonabe to expect that the specific relaxation mechanisms present in our islands (e.g. misfit dislocations, twin planes...) may also influence the domain wall displacement within our nanoislands. These factors could possibly account for the observed parallel vortex movement, although further evidence is required. A way to accomplish this objective is through more exhaustive micromagnetic simulations that consider all the unique ingredients of our system. These are currently underway, through a collaboration with Prof. A. Sánchez and Dr. C. Navau from the Universitat Autònoma de Barcelona (UAB).

In addition to simulations, there are a number of accessible experiments that could, in the near future, help unveil the nature of the vortex state in our solution-derived LSMO nanoislands. It would be very interesting, on one hand, to be able to apply higher in-plane magnetic fields. By reaching values of 500 mT[§], we would be sure of having saturated the islands in both directions. Although our calculations show that the applied 45 mT are enough to annihilate a vortex, we also mentioned that the numbers are a rough approximation and that should be regarded with caution. No doubts on reaching the saturation state would exist by applying a field as high as 500 mT. After having saturated the islands, decreasing the field towards the remanence state we would see whether the nucleation of the vortices happens similarly to what we have observed after reaching ∼45 mT, i.e. whether

[§]We know from SQUID measurements at 300 K that at such field values the whole nanoisland ensemble is fully saturated.

the core of the vortices shows only bright or, conversely, both bright and dark contrasts. Theory predicts that after saturating a nanomagnet the out-of-plane vortex core nucleates randomly either outwards or inwards. In our experiments up to date we have always recovered the initial bright core, as shown in the chapter. This is probably another property that is specific to our system, where the beveled-edge geometry breaks the symmetry of the geometry and somehow influences vortex nucleation. By applying very high field values this could be unambiguously ascertained.

Another experiment that would be interesting to perform is to carry out the same study as we did in here but from different starting conditions: we have mainly analyzed our system in remanence, after saturating tip and sample in opposite directions. Another option would be to investigate what is the relaxed magnetic structure achieved after having saturated the sample in-plane. In this case the exchange energy would favor in-plane magnetic moments, with the help of the flat nanoisland shape, while the magnetocrystalline anisotropy would pull the magnetization along the easy $< 111 >_{\mathrm{LSMO}}$ directions, and the demagnetizing field would tend to produce a flux-closure configuration. Although we know from micromagnetic simulations that the ground state of certain islands is the vortex state, a different, although metastable magnetic structure can also be achieved. Indeed, the magnetic structure dependency upon the magnetic history has already been reported for (0001) flat Co dots with a strong perpendicular anisotropy [257]: they have shown to display a vortex state in remanence after out-of-plane saturation (the ground state), and, by contrast, a single domain state (a local minimum), also in remanence, after in-plane saturation. Observing the behavior in our LSMO islands could help further unveiling the precise role of each of the energy terms. Furthermore, the broad range of aspect ratios found in our islands would allow us to observe the cross-over between different behaviors. For instance, regaining the vortex state after such in-plane saturation would underline the significance of the magnetocrystalline anisotropy in our system.